

Wetland mapping in East Asia by two-stage object-based Random Forest and hierarchical decision tree algorithms on Sentinel-1/2 images

Ming Wang^{a,d}, Dehua Mao^{a,*}, Yeqiao Wang^b, Xiangming Xiao^c, Hengxing Xiang^a, Kaidong Feng^{a,d}, Ling Luo^a, Mingming Jia^a, Kaishan Song^a, Zongming Wang^{a,e}

^a Key Laboratory of Wetland Ecology and Environment, Northeast Institute of Geography and Agroecology, Chinese Academy of Sciences, Changchun 130102, China

^b Department of Natural Resources Sciences, University of Rhode Island, Kingston, RI 02881, USA

^c Department of Microbiology and Plant Biology, Center for Earth Observation and Modeling, University of Oklahoma, Norman, OK 73019, USA

^d University of Chinese Academy of Sciences, Beijing 100049, China

^e National Earth System Science Data Center, Beijing 100101, China

ARTICLE INFO

Edited by Dr. Menghua Wang

Keywords:

Wetlands

East Asia

Object-based random forest

Hierarchical decision tree

Time series Sentinel-1/2 images

ABSTRACT

Accurate information on wetland extent in East Asia is essential to assess progress towards Sustainable Development Goals (SDGs) and the use of wetland resources, where wetlands benefit a quarter of the world's population and millions of wild birds in over three global migratory corridors. In this study, using 122,128 Sentinel-1 and 89,752 Sentinel-2 images acquired in 2021 available on the Google Earth Engine platform, we developed a novel two-stage classification for continental-scale wetland mapping and generated the first and up-to-date 10-m resolution wetland map of East Asia. Such a two-stage classification method, which integrates automatic sample generation and spatiotemporal features, combined an initial object-based random forest classifier with a subsequent hierarchical decision tree for secondary waterbody types. The resulting comprehensive map with 3 broad categories and 12 sub-categories in East Asia, named EA_Wetlands, achieved over 88% overall accuracy. According to EA_Wetlands, the total wetland area in this region is 481,802.49 km², mainly distributed in Northeast China and the Qinghai-Tibet Plateau (41.02%). Of all wetlands in East Asia, about 68.26% are inland wetlands. The highest proportion (29.67%) is identified for inland marsh among 12 sub-categories. Among five countries, China has >88% of the total wetland resources in East Asia, followed by Mongolia (3.57%). South Korea has the largest ratio between wetland and national land areas (10.43%). EA_Wetlands, as the first 10-m resolution wetland data product, will have great applications and benefit wetland conservation and policy management. It will be a critical support for evaluating the implementation of wetland-related international conventions at country and continental scale in East Asia.

1. Introduction

Wetlands are among the world's most productive ecosystems and play an irreplaceable role in maintaining water balance, reducing the risk of floods and droughts, improving water quality and protecting biodiversity (Mao et al., 2020). Climate change and intensive human activity have profoundly altered the global hydrological cycle, resulting in a spatiotemporal redistribution of water resources, which led to a drastic reduction of wetland areas and a severe deterioration of their ecosystem functions and services (Mao et al., 2022; Wang et al., 2012; Zedler and Kercher, 2005). East Asia includes China, Mongolia, Japan, North Korea, and South Korea, covering 28% of the Asian continent and

roughly 25% of people worldwide. The rich wetland resources in East Asia have been experiencing severe losses and degradations due to human activities and climate change (Davidson and Davidson, 2014; Mao et al., 2018; Matsushita and Fukushima, 2009). Previous studies have provided valuable datasets of various wetland categories in East Asia (Betbeder et al., 2014; Gong et al., 2010; Zhang et al., 2022). However, these data are either outdated or inadequate for wetland planning and management, particularly due to limitations in spatial resolutions, scale consistency and differentiation in wetland types. Therefore, it is necessary to explore a feasible method for timely and large-scale wetland mapping that can produce an up-to-date wetland map with fine spatial resolution and multiple categories.

* Corresponding author.

E-mail address: maodehua@neigae.ac.cn (D. Mao).

<https://doi.org/10.1016/j.rse.2023.113793>

Received 27 March 2023; Received in revised form 25 August 2023; Accepted 26 August 2023

Available online 4 September 2023

0034-4257/© 2023 Elsevier Inc. All rights reserved.

Various sources of satellite data have been applied to identify wetlands worldwide (Baghdadi et al., 2001; Tana et al., 2013; Wang et al., 2023). Among which Landsat series data have been extensively used in mapping large-scale wetlands (Jin et al., 2017; Wang et al., 2020). Nevertheless, there are several limitations when mapping large-scale wetlands using Landsat images. First, Landsat imagery with a medium resolution (30-m) could not accurately identify small wetland areas. Second, Landsat's temporal resolution, 8–16 days, may affect high-quality observations particularly in low latitudes regions, due to cloud contaminations for wetlands with distinct temporal variations such as salt marsh and tidal flat (Jia et al., 2021). Open access and freely available Sentinel-1/2 images have been increasingly employed in wetland classification in recent years because of the 10-m spatial resolution and revisits interval of 2–5 days (Ashourloo et al., 2022; Wang et al., 2023). Such fine spatial resolution and dense temporal coverages of Sentinel-1/2 images offer the opportunity to map various wetland categories and capture their seasonal variations (Feng et al., 2022). Additionally, combination of Sentinel-1 SAR data with Sentinel-2 MSI optical images can improve wetland mapping accuracy by increasing good observations and providing more features for classification. Although several studies for wetland mapping used Sentinel-1/2 imagery (Kaplan and Avdan, 2018; Mahdianpari et al., 2020), applications towards extensive areas and improved accuracy need to be explored to support sustainable management and conservation of wetlands.

To date, diverse supervised machine learning methods such as support vector machines, Random Forest (RF), as well as deep learning have been widely applied in large-scale wetland mapping (Hosseiny et al., 2022; Zhao et al., 2022). Most of these studies, at national or continental scales (Liu et al., 2022; Peng et al., 2023), are pixel-based classifications using only features derived from pixels, which may not be sufficient to accurately identify wetlands with high environmental heterogeneity. By segmenting satellite imagery into homogeneous objects, object-based image analysis (OBIA) can provide more useful features for wetland mapping that individual pixels lack, such as shape, texture, and context, and support the option of fusing multi-source data to enhance the classification accuracy (Blaschke, 2010). Numerous studies have shown that object-based machine learning methods have superior efficiency and robustness in terms of both computational overhead and model performance for landscape classification (Gong et al., 2019). As a non-parametric supervised learning approach for classification and regression problems (Kotsiantis, 2013), a decision tree demands considerable prior knowledge that hampers its speed and precision in classifying multiple landscape categories over large areas. Yet, it has been proven effective in distinguishing various types of wetlands, particularly the waterbody, by synthesizing multiple features (e.g., spectral, landscape, temporal change, and environmental features) and creating associated classification rules (Mao et al., 2020). It is necessary to effectively combine the advantages of object-based machine learning and decision tree classification, and further to develop a two-stage classification framework for fine mapping of wetlands over a large area.

Obtaining sufficient and accurate training samples and selecting reliable spatiotemporal features that reflect the dynamic of wetland ecosystems remains the greatest challenge for wetland mapping in extensive continental scale. Most previous studies construct training sample sets through ground surveys, visual interpretation based on high-resolution imagery, and various dataset, such as public sample databases, historical sample datasets, and land cover datasets (Gong et al., 2010; Li et al., 2022a). These samples from various sources and dates were usually used directly or validated by visual interpretation, which might create significant uncertainty. Some studies have proposed sample migration methods using distance measures, such as the Euclidean Distance (ED) and Spectral Angle Distance (SAD), to tackle this problem (Huang et al., 2020; Wang et al., 2022). These methods, however, typically perform well in landscapes with simple characteristics and rely on empirical thresholds, which may not be appropriate to provide valid samples for wetland mapping. In addition, due to the high

environmental heterogeneity and temporal variations of wetland landscape, misclassification may occur in wetland mapping process when only spatial features derived from a single image are used instead of considering their distinct temporal variations. As a result, an improved approach that automatically generates training samples and fully exploits temporal change features is in demand for fine wetland mapping at a large scale.

Given these issues, the objectives of this study are to: (1) develop an improved approach for large-scale wetland mapping based on time-series Sentinel-1/2 imagery; (2) apply the approach on the GEE platform to produce the first comprehensive wetland map of East Asia in 2021 with a 10-m spatial resolution, named EA_Wetlands; (3) assess the accuracy of the EA_Wetlands map and compare it with other available products; and (4) analyze the spatial pattern of wetlands in East Asia and the potential application of the EA_Wetlands map. The developed method and the generated result are expected to provide a reference for wetland resource management and support the evaluation of wetland-related targets in the Sustainable Development Goals (SDGs).

2. Materials

2.1. Study area

East Asia covers an area around 12 million km², or roughly 9% of the world's land (Matsushita and Fukushima, 2009). It is the most densely populated region in the world and one of the most active and influencing areas in global economics. East Asia has terrain changes from the Tibetan Plateau to the coast of Pacific Ocean and encompasses climates from the temperate zone in the north to the subtropical and tropical zones in the south. It has abundant and diverse wetland resources and is home to several Asia's significant rivers and lakes. The wetlands here serve as critical migration corridors and sustain biological diversity. In this study, we divided the East Asia into 11 ecoregions based on the watershed and administrative boundaries. The ecoregions are named Mongolia (MN), Northeast China (NEC), Inner Mongolia-Xinjiang Plateau (MXP), Lower and middle reaches of the Yellow River (YER), Qinghai-Tibet Plateau (QTP), Yunnan-Guizhou Plateau (YGP), Lower and middle reaches of the Yangtze River (YAR), Southeast and South China (SSC), Korean Peninsula (KP), Japan (JPN), and Coastal area of East Asia (COAST) (Fig. 1). Due to its unique ecosystem and geographic conditions, the coastal area was separated into a single ecoregion (COAST), which include the zone between a 20-km buffer line inland and a 6-m isobaths buffer line offshore.

2.2. Data sources

2.2.1. Satellite images and preprocessing

A total of 211,885 Sentinel-1 SAR and Sentinel-2 MSI images covering the entire East Asia in 2021 and available in the GEE platform were employed in this study. Among those included 122,128 dual-polarized (VV + VH) Sentinel-1 SAR GRD images in ascending and descending orbit and 89,752 Sentinel-2 MSI images. Note that 27 Sentinel-1 images from 2018 were used for areas (south-central MN) that lacked observations in 2021. A Refined-Lee filter (Yommy et al., 2015) was employed for each Sentinel-1 image to reduce the impact of speckle noise. The QA60 bitmask band of each Sentinel-2 image was applied to mask the low-quality observations caused by cloud. Fig. 2 presents the spatial distributions and histograms of available Sentinel-1/2 data pixels, respectively. >60 Sentinel-1 observations were available for over 90% of the pixels in 2021, while >50 good-quality Sentinel-2 observations were obtained for over 70% of the pixels (Fig. 2A and B). Then, all the processed images were integrated into Sentinel-1/2 dense time-series data, which were utilized to provide temporal variation information for wetland classification. Using the GEE temporal aggregation function, each pixel across the time-series was further aggregated into a single observation by computing their median value, resulting in

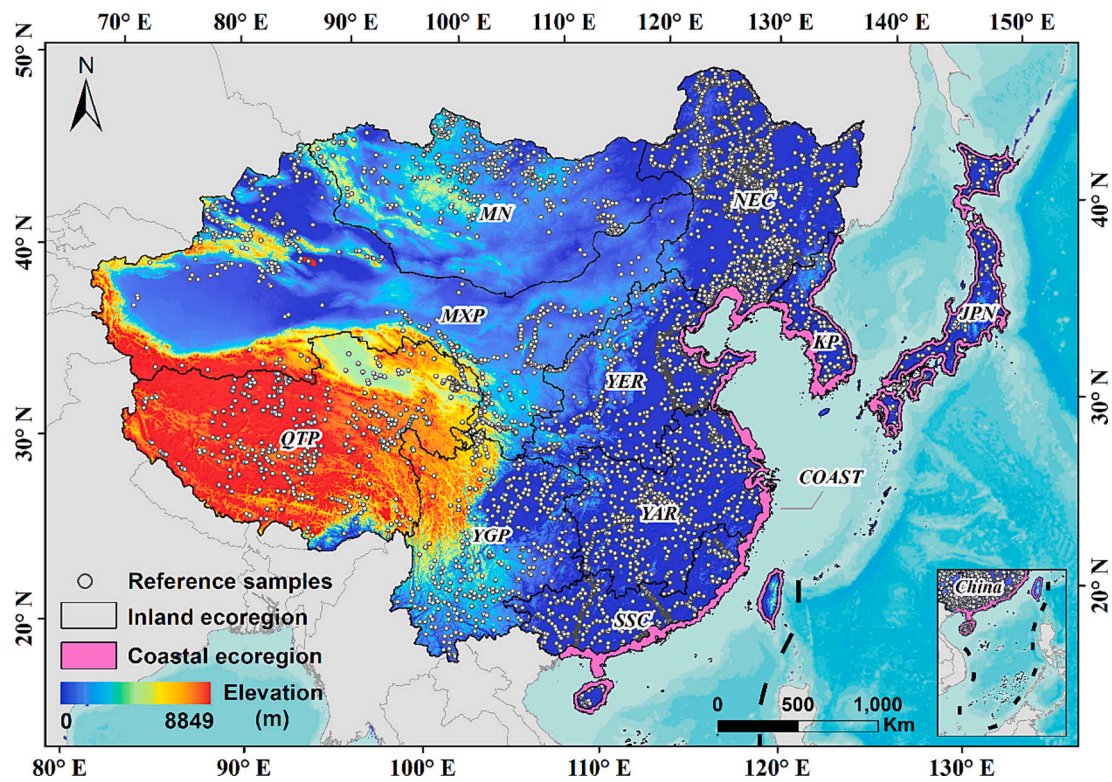


Fig. 1. Spatial distribution of 11 ecoregions and reference sample locations in the study area.

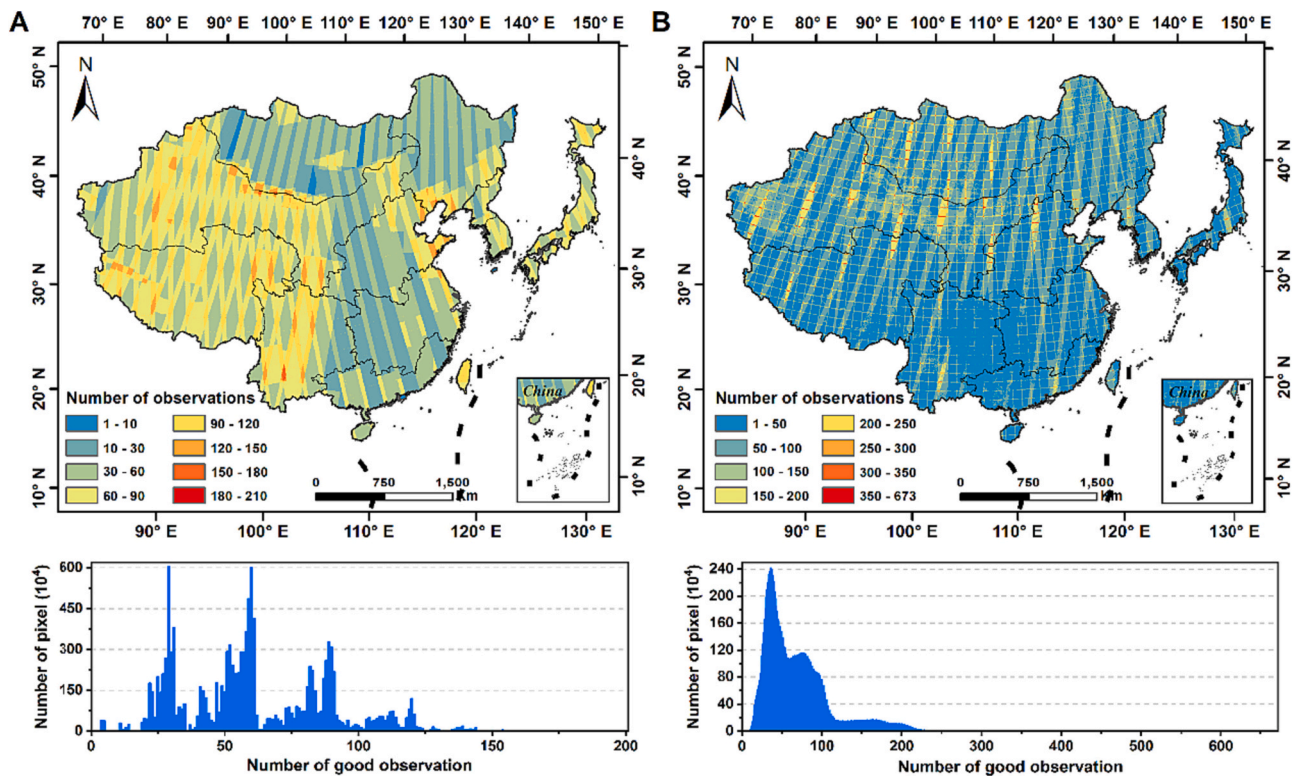


Fig. 2. Spatial distribution and the number of observations across East Asia in 2021 by Sentinel-1 (A) and Sentinel-2 (B), respectively. The histograms illustrate the number of observations in good data quality accordingly.

Sentinel-1/2 composite images in 2021. Instead of the original images, using composite images generated by temporal aggregation significantly reduced data size, improved image quality, and allowed faster and more

efficient image analysis (Tassi and Vizzari, 2020).

2.2.2. Reference sample data and preprocessing

Using digital cameras, hand-held geographic positioning systems (GPS), and unmanned aerial vehicles (UAV), we collected 15,808 wetland and non-wetland samples through a series of field surveys in China from 2015 to 2021. To ensure the accuracy of these samples, we removed samples that were no longer valid in 2021. These samples were used to select the optimal features for wetland classification and to automatically generate more training samples. Specifically, 70% of these samples were randomly selected to help generate new training samples using the automated sample generation method proposed in this study, and the remaining 30% were used to validate its performance. Finally, all of these reference samples were used to train the classification model along with the new training samples generated by the automatic generation method (Section 3.2). In addition, using the latest Google Earth images, we visually mapped 1000 sample polygons for different categories of waterbody, which were ultimately used to construct and validate the hierarchical decision tree for waterbody subdivision.

2.2.3. Auxiliary data

A digital elevation model (DEM) with a 30-m spatial resolution from the Shuttle Radar Topography Mission (SRTM) was utilized to produce topographic information such as elevation, slope, and surface roughness. The 6-m isobaths buffer line offshore was obtained from the ETOPO1 dataset (Amante and Eakins, 2009), which was used to determine the coastal area in this study. The spatial location of dams around the waterbodies, obtained from OpenStreetMap and the Global Georeferenced Database of Dams (GOODD) (Table 1), helped us to classify the waterbodies. Several existing datasets (Table 1) with various scales and spatial resolutions, including the land cover and thematic data for wetland and non-wetland, were collected for automatic sample generation in this study. Among these, the wetlands result generated in this study was contrasted with five datasets, i.e., ESA_Worldcover (Zanaga et al., 2022), CAS_Wetlands (Mao et al., 2020), China_Tidal Flat (Jia et al., 2021), China_CAP (Wang et al., 2023), and CAS_Mangroves (Jia et al., 2018).

3. Methods

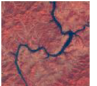
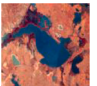
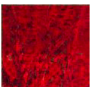
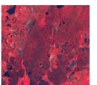




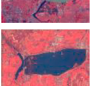



This study classified the wetlands in East Asia into 3 broad categories

Table 1
Auxiliary datasets used in this study.

Dataset type	Name	Resolution	Date
Land cover	ESA_Worldcover (Zanaga et al., 2022)	10-m	2021
	FROM-GLC10 (Gong et al., 2019)	10-m	2017
	DynamicWorld (Brown et al., 2022)	10-m	2015 ~ now
	China_Cover (Wu, 2014)	30-m	2015
	MCD12Q1	500-m	2001–2006
	CAS_Wetlands (Mao et al., 2020)	30-m	2015
	Global Lakes and Wetlands Dataset (Lehner and Döll, 2004)	1-km	–
Wetlands	China_Tidal Flat (Jia et al., 2021)	10-m	2019
	Global Intertidal Change (Murray et al., 2019)	30-m	1984–2016
	CAS Coastal Aquaculture (Ren et al., 2019)	30-m	1986–2016
	China_CAP (Wang et al., 2023)	10-m	2016–2021
	CAS Mangroves (Jia et al., 2018)	30-m	2015
	Global Mangrove Watch (Bunting et al., 2018)	30-m	1984–2016
	JRC-GMW (Pekel et al., 2016)	30-m	1984–2019
Others	EULUC-China-2018 (Gong et al., 2020)	30-m	2018
	GAIA (Gong et al., 2020)	30-m	1985–2018
	GFSAD1000 (Thenkabail et al., 2012)	1000-m	2000–2021
	GOODD (Mulligan et al., 2020)	–	2017

and 12 sub-categories (Table 2) based on the wetland definition by the Ramsar Convention and the wetland classification systems used by various studies (i.e. Gong et al., 2010; Mao et al., 2020). In addition, other main land cover types were added as the non-wetland categories for classification, including woodland, grassland, barren land, cropland, built-up land, and snow/ice. Applying this classification system, we implemented a novel two-stage classification for mapping different categories of wetlands at a continental scale. First, we developed an object-based RF classification by integrating automatic sample generation and spatiotemporal features. In this stage, the wetlands in East Asia were classified into waterbody, inland/coastal marsh, inland/coastal swamp, and tidal flat, respectively. Secondly, waterbody from the initial results was further separated into lake, river, pond/reservoir, canal/channel, coastal waterbody, coastal aquaculture pond, and salt pan, respectively, using hierarchical decision tree classification. Specifically,

Table 2
The classification system for mapping wetlands in East Asia.

Category I	Category II	Description	Image Example
Inland Wetland	River	Natural linear waterbody with flowing water in inland areas	
	Lake	Natural polygon waterbody with standing water in inland areas	
	Inland swamp	Natural wetland with dominant woody vegetation in inland areas including forested wetland and shrub wetland	
	Inland marsh	Natural wetland with dominant herbaceous vegetation in inland areas	
	Coastal swamp	Natural wetland with dominant woody vegetation in coastal areas including forested wetland and shrub wetland	
	Coastal wetland	Natural wetland with dominant herbaceous vegetation in coastal areas	
Human-made wetland	Tidal flat	The intertidal flat with no or very low vegetation coverage including sand beach, rocky shore, and coral reef	
	Coastal waterbody	Natural waterbody in coastal area, such as the lagoon, shallow marine water, and estuarine water	
	Reservoir/pond	Artificial polygon waterbody with standing water generally with obvious dam	
	Canal/channel	Artificial linear waterbody with flowing water, generally with the obvious dam or the straight boundary	
	Salt pan	Artificial flat depression ground covered with salt and other minerals close to sea	
	Coastal aquaculture pond	Polygon waterbody used for aquaculture with regular shape and close to river or sea	

Note: the image examples in displays are Sentinel-2 MSI data (R:G:B=Band 8:4:3) acquired in 2021.

we divided the wetland mapping process into four major components: extraction and selection of spatiotemporal features, automatic generation of training samples, wetland mapping using a two-stage classification approach, and accuracy evaluation (Fig. 3).

3.1. Extraction and selection of spatiotemporal features

To improve the spatial detail of images, a total of 86 spatiotemporal variables were generated for mapping wetlands (Table 3). Multiple spatial variables were extracted from Sentinel-1/2 composite images in 2021, including intrinsic bands of Sentinel-1/2 imagery, 5 polarization indices, 8 spectral indices, 16 red-edge indices, 3 main components of the tassell cap transform (Wang et al., 2022), 5 texture features, and 3 topographic features. Besides extracting the widely used variables above, this study reconstructs the time-series of NDVI, NDWI, VV, and VH from the dense time-series Sentinel-1/2 images using the Harmonic Analysis of Time Series algorithm (HANTS) (Jakubauskas et al., 2002; Zhou et al., 2015). Then, various temporal variation features, including maximum, minimum, median, mean, standard deviation, amplitude, and phase, were extracted to reflect the seasonal variation patterns of different landscapes (Fig. 4). HANTS can link the spatial distribution and temporal variation patterns of landscapes, whilst reconstructing the time series variation curves to truly reflect the cyclical variation patterns of landscapes (Fig. 4A). The above temporal features clearly enhance the differences between wetlands and other easily confused land cover types (Fig. 4C), which is difficult to achieve using only standard spatial features (Fig. 4B). Combined with the reconstructed NDVI, NDWI, VV, and VH time series images and the OTSU algorithm (Otsu, 1979), we also extracted the frequency of landscape's vegetation and water coverage throughout the year (Table 3). Those were used to characterize the

spatial and temporal dynamic information related to vegetation or water bodies.

A large number of input variables in classification may lead to multicollinearity and information redundancy, hence increasing the complexity of the classifier and degrading its performance (Zou et al., 2015). In this study, the Relief-F algorithm (Kononenko, 1994) was employed to filter the usable features from the high-dimensional data for mapping wetlands and further to minimize feature redundancy and enhance classifier performance. The Relief-F algorithm is a feature selection algorithm that is efficient and robust against outliers, which have been widely utilized in numerous studies on optimal feature selection (Wang and Makedon, 2004). Since the geographic conditions and land cover types of each ecoregion vary, we applied the Relief-F to determine the optimal features for each ecoregion using their samples (Section 2.2.2) and all spatiotemporal features, respectively.

3.2. Automatic sample data generation

Although we have conducted multiple field surveys and collected some reliable sample data (Section 2.2.2), these samples were not sufficient for mapping wetland across East Asia. Therefore, we implemented a method for automatically generating training samples based on multi-source data to generate a sample set suitable for continental-scale wetland classification. The main steps of the method are described below.

3.2.1. Determining potential sample selection regions

The potential sample selection regions for various wetland and non-wetland categories were determined through multi-source datasets and spatial overlay analysis. First, we extracted the spatial extent of each

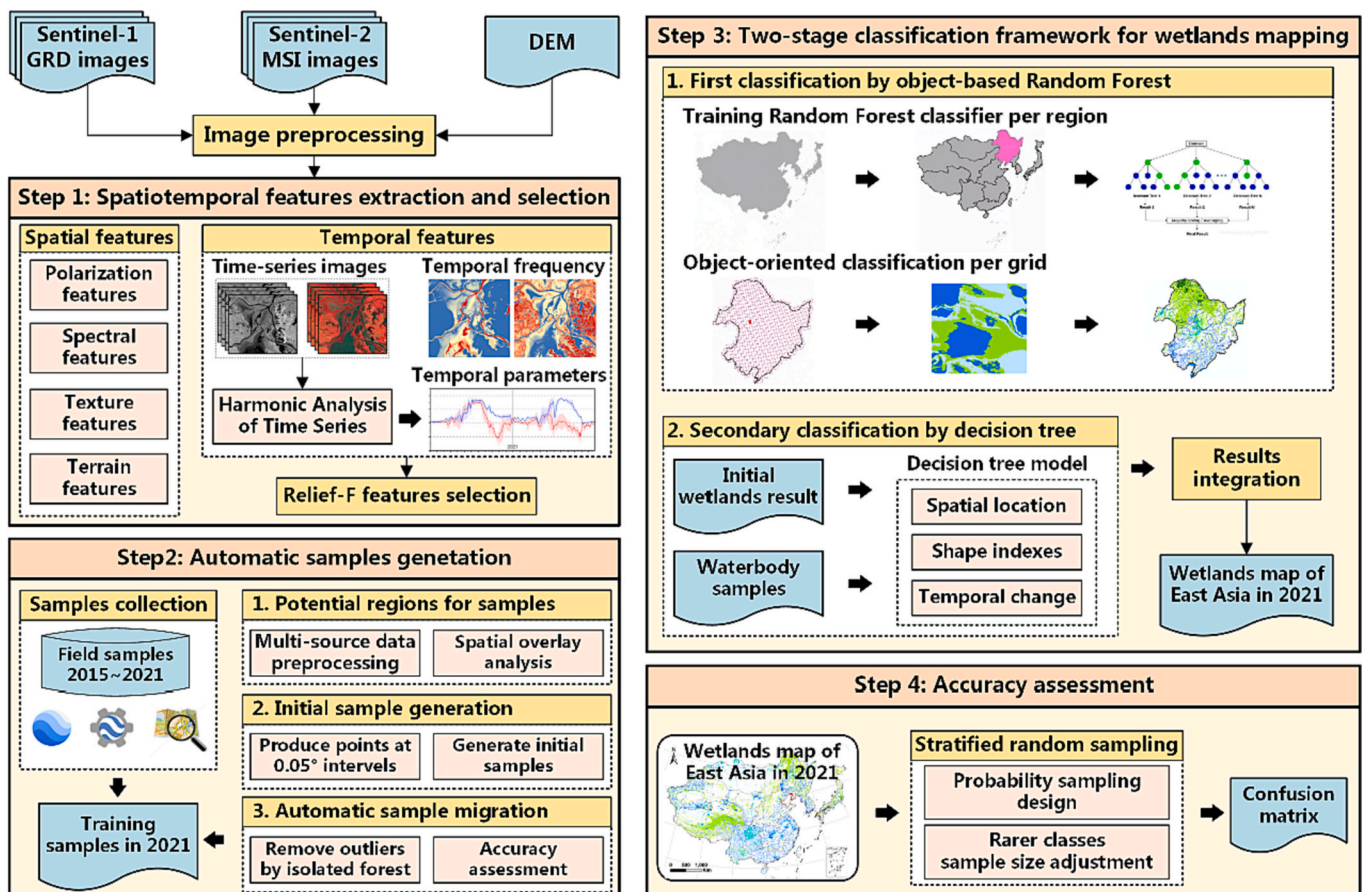


Fig. 3. General workflow for wetland mapping.

Table 3
Spatiotemporal features extracted in this study.

Feature category	Feature name (Number)	Datasource
Polarization	Polarization bands	VV, VH (2)
	Polarization indexes	VV + VH, VH-VV, NDV_VV, NDV_VH, VH/VV (5)
	Spectral bands	B1 ~ B12 (13)
	Spectral indexes	NDVI, EVI, DVI, GNDVI, NDWI, mNDWI, NDBI, NDMI (8)
Spectral		NDVire1, NDVire1n, NDVire2, NDVire2n, NDVire3, NDVire3n, PSRI, Clre, NDre1, NDre1m, NDre2, NDre2m, SRre1, SRre2, MSRre, MSRren (16)
	Red edge indexes	
	Tasseled cap transform	Brightness, Wetness, Greenness (3)
		ASM, Contrast, Entropy, Correlation, Dissimilarity (5)
Texture	–	Sentinel-2
Terrain	–	Elevation, Slope, Roughness (3)
		DEM
Temporal	HANTS_NDVI	NDVI_min, NDVI_max, NDVI_mean, NDVI_median, NDVI_std, NDVI_phase, NDVI_amplitude (7)
	HANTS_NDWI	NDWI_min, NDWI_max, NDWI_mean, NDWI_median, NDWI_std, NDWI_phase, NDWI_amplitude (7)
		Time-series
	HANTS_VV	VV_min, VV_max, VV_mean, VV_median, VV_std, VV_phase, VV_amplitude (7)
		Sentinel-1/ 2
	HANTS_VH	VH_min, VH_max, VH_mean, VH_median, VH_std, VH_phase, VH_amplitude (7)
	HANTS_NDVI_Frequency	NDVI_frequency, NDWI_frequency, VV_frequency, VH_frequency (4)

Note: The NDWI used in this study was calculated using the green and near-infrared bands of the Sentinel-2 image.

wetland and non-wetland category from the different datasets as described in Section 2.2.3. Then, the spatial overlay method was used to obtain the intersection areas among the various spatial extents of specific categories extracted from different products. These overlapping regions derived from multiple datasets greatly reduce the difference between various datasets and can be used as possible sample selection regions. Finally, the potential sample selection regions for various categories were determined.

3.2.2. Automatic generation of initial training samples

To obtain sufficient sample data for wetland classification, we generated initial samples covering the entire study area based on various potential sample selection regions described above. First, we produced uniformly dispersed points at 0.05-degree intervals across the study area. Then, based on their locations, the points within each potential sample selection regions were classified as the corresponding sample type. Finally, samples outside of the potential sample selection regions were eliminated and the initial sample data were generated.

3.2.3. Automatic sample migration by isolated forest algorithm

The initial samples generated in the previous step are likely to be inconsistent due to differences in spatial resolution, acquisition time, and classification accuracy across the data products. This study employed the Isolated Forest algorithm (iForest) to identify and eliminate outliers in all categories of training samples for wetland mapping. The iForest is an effective data anomaly detection method that can handle high-volume and high-dimensional data (Liu et al., 2012). It computes an anomaly score for each value, which indicates how different it is from the normal. In this study, we mixed the field samples described in Section 2.2.2 with the initial samples, and then detected the anomaly samples using iForest, which can further increase the

discrimination between outliers and normal values to improve the detection accuracy. Finally, the anomaly scores of all training samples are measured on optimally selected spatiotemporal variables using iForest, and samples with anomaly scores within the 5% probability range before and after are determined as outliers and be eliminated.

3.2.4. Accuracy assessment of automatic sample generation

To verify the accuracy of the automatically generated samples, we constructed two sample sets using random sampling both containing two sample groups. The first set contains samples from both the automatically generated samples and the field samples (Section 2.2.2). The second set contains two different sample groups from field surveys alone. Each group has the same number of samples (1200, with 100 per category). We calculated the Euclidean Distance (ED) and Spectral Angular Distance (SAD) between the samples of both groups within each set, and then compared these distances to verify the accuracy of the automatically generated samples in this study.

3.3. Two-stage classification for wetland mapping

3.3.1. Generation of homogeneous landscape objects by image segmentation

The Simple Non-Iterative Clustering (SNIC), an efficient super pixel image segmentation algorithm (Achanta and Süsstrunk, 2017), was used to generate homogeneous landscape objects in this study. Due to the strong environmental heterogeneity and spatiotemporal fluctuation of wetlands, using an empirical segmentation threshold is insufficient to accurately extract various wetlands with varying sizes and shapes. A low threshold will drastically increase computing work, whereas a high threshold will result in inhomogeneous results. Thus, an effective approach for optimal segmentation threshold determination was designed in this study. There are four steps to determine the threshold: (1) Select small, highly fragmented patches as typical objects for each wetland category, since they are typically the most direct factor affecting segmentation accuracy (Fig. 5A). (2) Calculate the standard deviation of NDVI (NDVI_SD) within the object to measure its homogeneity, and further construct the change curve of NDVI_SD at different segmentation scales (5–100) (Fig. 5B). (3) Determine the critical point on NDVI_SD curve for each wetland type using the sliding window algorithm, i.e. the segmentation threshold where the homogeneity of the objects begins to vary. (4) The smallest value among the critical threshold of wetland type was ultimately chosen as the optimal segmentation scale, as it enables effective segmentation of even the smallest wetland patches. According to the above method, the critical threshold for each wetland type in this study ranged from 18 to 35, and the optimal segmentation threshold for mapping wetlands in East Asia was determined to be 18 (Fig. 5B).

3.3.2. First-stage classification using object-based RF algorithm

Based on the spatiotemporal features as well as the training samples described in Section 2.2.2 and 3.2, the object-based RF algorithm was used for the initial classification of wetlands. First, independent RF classifiers were trained for each ecoregion. Second, each ecoregion was partitioned into $0.3^\circ \times 0.3^\circ$ grids, and image segmentation was conducted per grid using the SNIC. Object-based classification was then performed for each ecoregion using their classifier. Finally, the initial wetland map, including the water body, inland marsh, coastal marsh, inland swamp, coastal swamp, and tidal flat, was generated by integrating the results from all ecoregions.

3.3.3. Second-stage classification by hierarchical decision tree

In this study, geographic location, area, shape, topography, and temporal change features of waterbody objects were jointly employed to create a hierarchical classification tree that subdivided waterbodies based on the previous classification results (Fig. 6A). We determined its rule sets and thresholds by the sample polygons described in Section 2.2.2. First, we divided the water body objects into coastal and inland

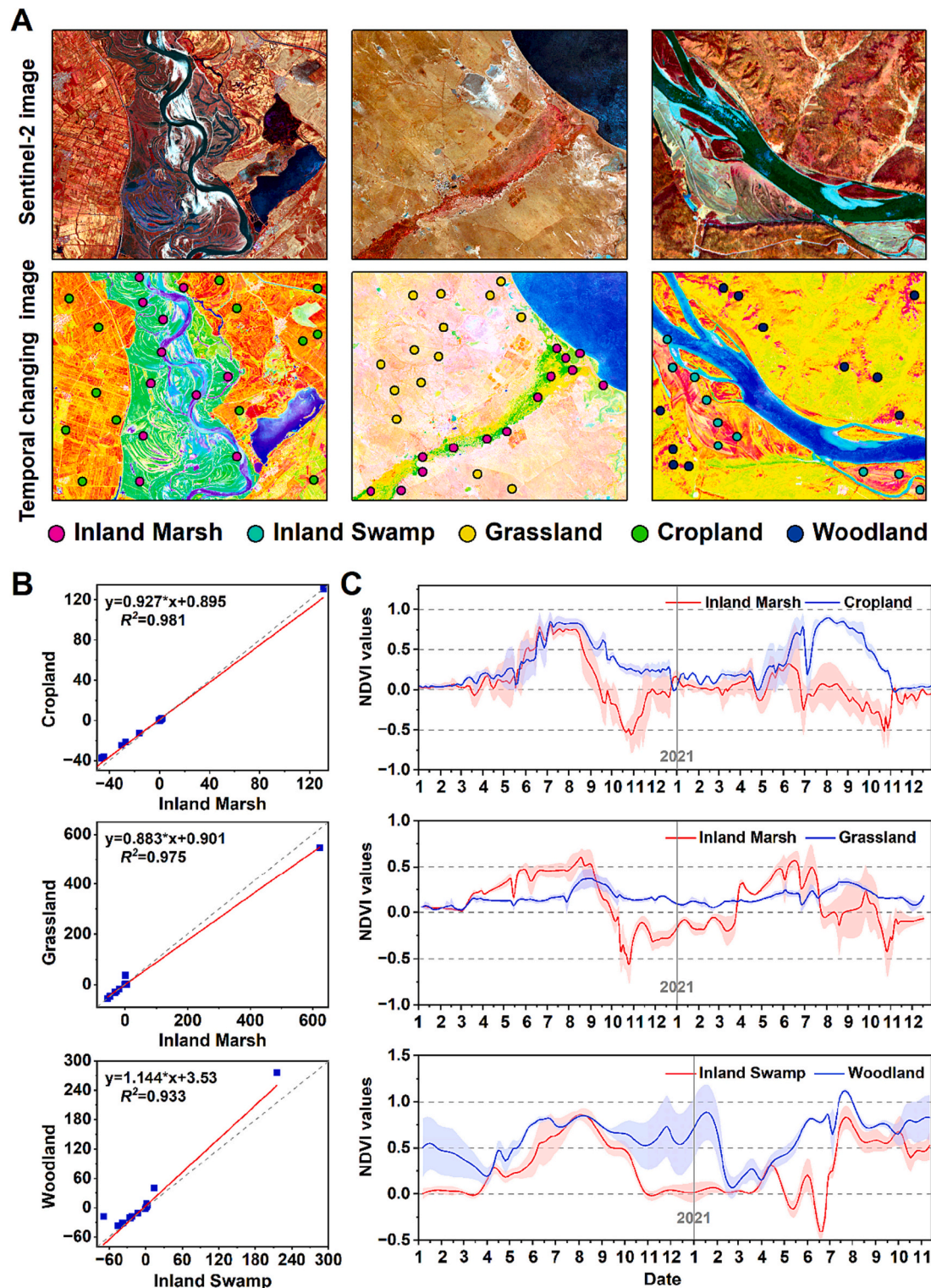


Fig. 4. Temporal features extracted in this study, (A) presents the Sentinel-2 data (R:G:B=Band 8:4:3) and their temporal changing images (compound by the NDVI amplitude and NDVI phase images) reconstructed by HANTS, (B) shows the correlation of spatial features between the wetland and non-wetland samples, and (C) shows the difference of temporal features between the wetland and non-wetland samples.

ones according to the extent of the coastal area, i.e., the zone between a 20-km inland line and a 6-m isobath line. For the inland waterbodies, we first used shape indices, including landscape shape index and compactness, to classify them into linear and polygonal categories. Then, linear water bodies were further subdivided into river and canal/channel by judging whether they were regular in shape and contained dams. Among

the polygonal categories, we determined those with an area larger than 1 km² and without obvious dams as lakes, and the rest as reservoirs/ponds. For the coastal waterbody objects, we first classified them as natural or artificial by judging whether they were regular in shape and contained obvious dams. We determined the natural part as coastal water bodies. Then, we classified artificial waterbodies in the coastal

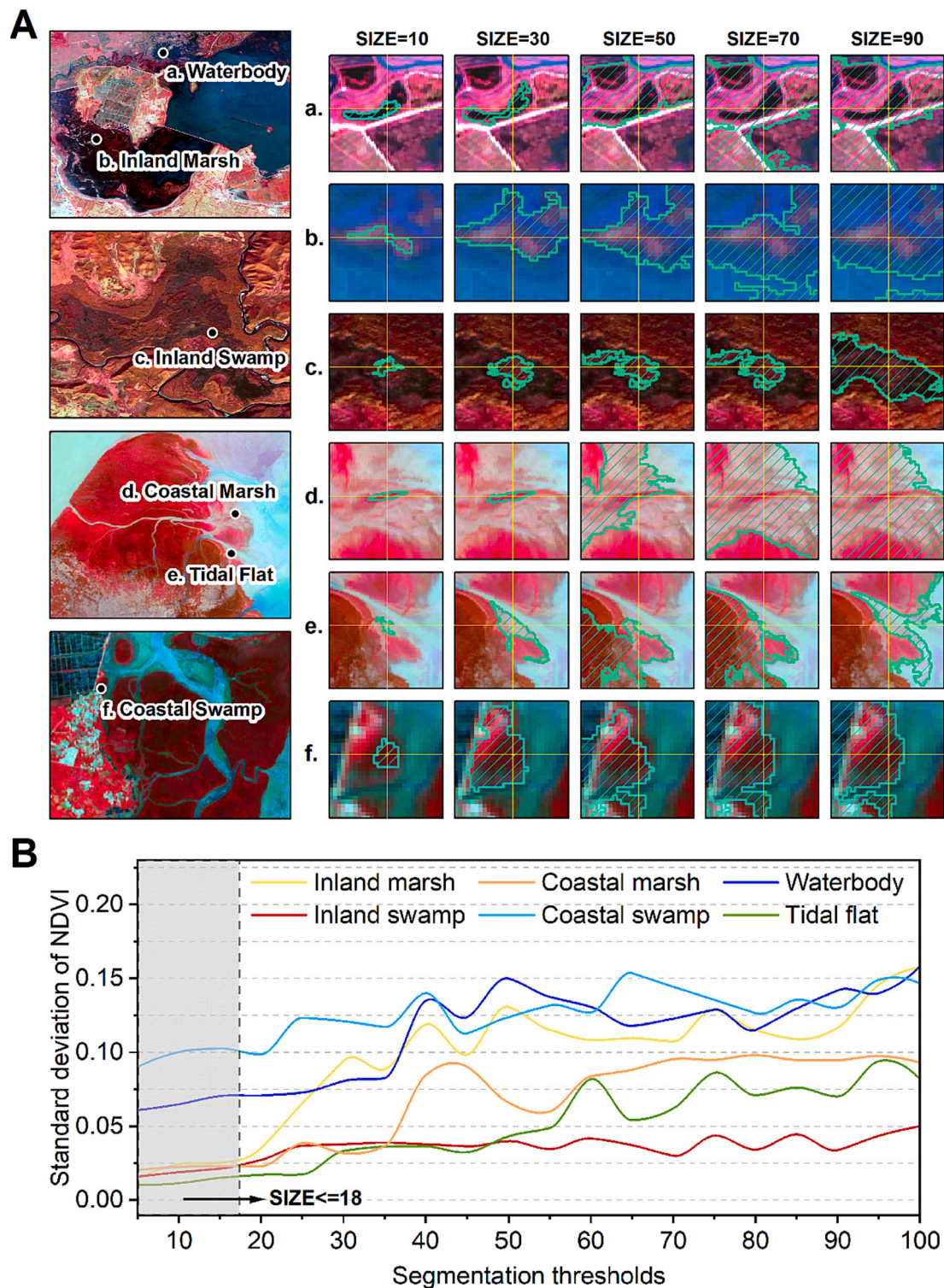


Fig. 5. The determining process of optimal SNIC segmentation scale. A shows the segmentation result for various wetlands at different segmentation scales, and B presents the NDVI_SDCV curves for various wetlands at different segmentation scales.

area into coastal aquaculture ponds and salt pans based on their temporal change characteristics. Aquaculture ponds and salt pans are usually undergo periodic drainage and storage of water in a year, and salt pans exhibit more pronounced periodic changes compared with aquaculture ponds.

3.4. Accuracy assessment of wetland classification results

In this study, stratified random sampling method was employed to assess the accuracy of the 2021 wetland map of East Asia. Firstly, the resultant wetland map was partitioned into 18 strata including 12 wetland categories and 6 non-wetland categories. Secondly, referencing the previous studies (Olofsson et al., 2014), we estimated the total number of random samples (41,742) and allocated the corresponding

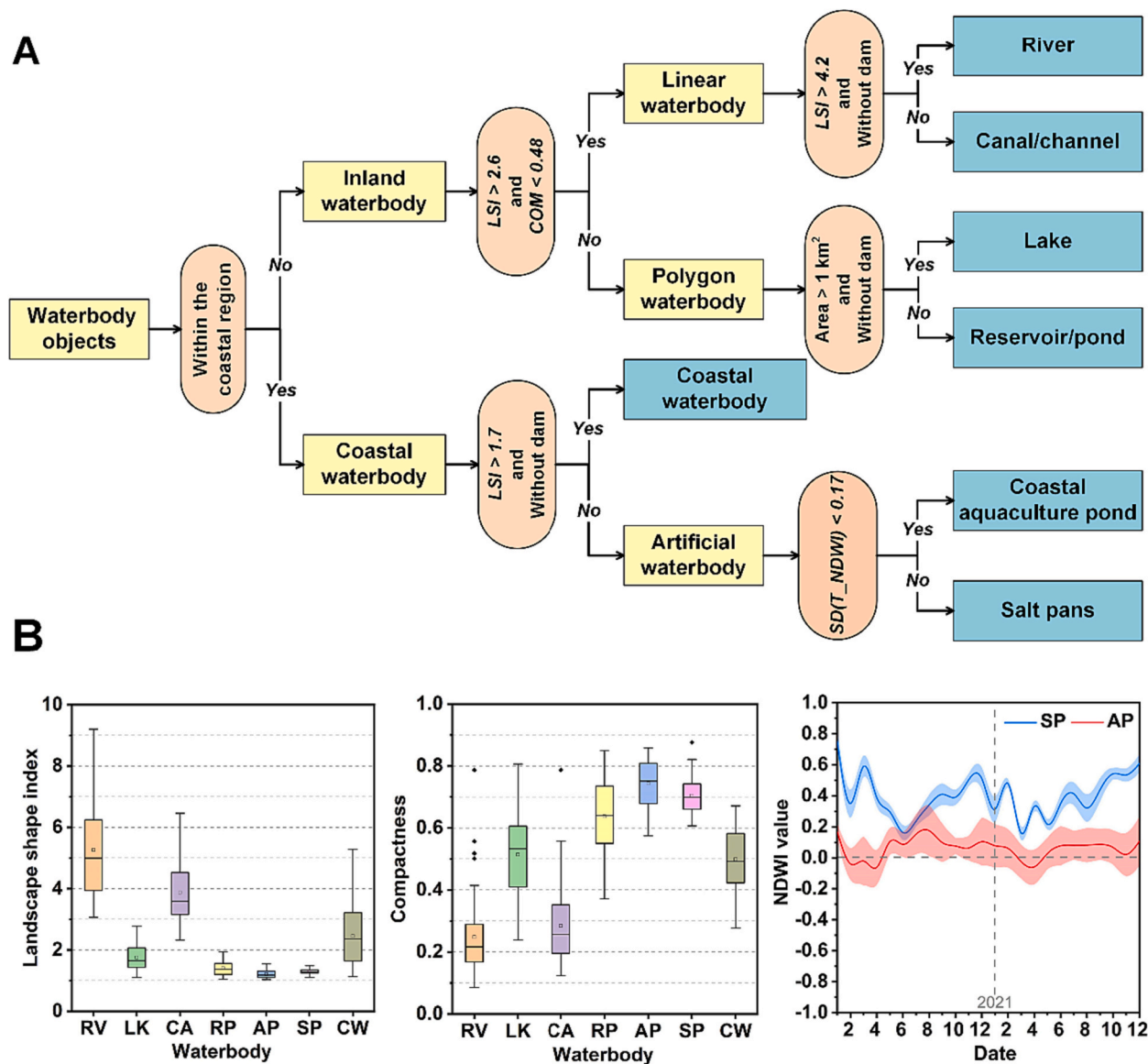


Fig. 6. Hierarchical decision tree for waterbody classification: (A) shows the decision tree model. Where LSI and COM represent the landscape shape index and the compactness, respectively. $SD(T_NDWI)$ is the standard deviation of the NDWI change over one year. (B) shows the COM, LSI, and time-series NDWI value among various waterbody. RV: river, LK: lake, CA: canal/channel, RP: Reservoir/pond, AP: coastal aquaculture pond, SP: salt pan, CW: coastal waterbody.

sample size to each stratum according to their area proportion. In particular, we adjust the allocation by increasing the sample size for the rarer classes, such as tidal flat, salt pan, and snow/ice, making the sample size per stratum more equitable than what would result from proportional allocation. Then, random points were generated in each stratum according to the sample size allocation, and each sample point was visually examined and interpreted using high-resolution Google Earth images. Finally, a confusion matrix of the resultant wetland map was created to evaluate the accuracy of the results, and their standard errors were further calculated to quantify sampling variability. The accuracies were presented with a 95% confidence interval. To assess the accuracy of the shapes and areas of different wetlands derived from our map, we also compared our mapping results with five wetland datasets.

4. Results

4.1. Performance of automatic sample generation method

A total of 48,123 sample points were automatically generated using

the developed method (Fig. 7). Wetland and non-wetland samples accounted respectively for 48.25% and 51.75% of the total generated samples, respectively. Waterbody and inland marsh samples comprised 52.13% of all wetland samples, whereas coastal swamp samples were the least abundant (7.43%). Due to the apparent disparities in area and landscape type among ecoregions, the sample sizes differed significantly (Fig. 7B), with the most samples in the QTP (18.03%), followed by the NEC (15.75%), and the fewest in the KP (2.21%).

Using the random sampling proposed in Section 3.2.4, we evaluated the similarity of the samples generated by the automatic method (Auto_S) and the samples collected by a series of field surveys (Field_S) for all spatiotemporal features. Fig. 8 compares the ED and SAD of these samples. The results show that the automatically generated samples in this study and the field samples are highly consistent for all features, with similar values between ED (Auto_S, Field_S) and ED (Field_S, Field_S) and between SAD (Auto_S, Field_S) and SAD (Field_S, Field_S). This indicates reliable accuracy of the automatic sample generation method for different sample types. In particular, vegetated wetlands (marshes and swamps in inland and coastal areas) have larger EDs and

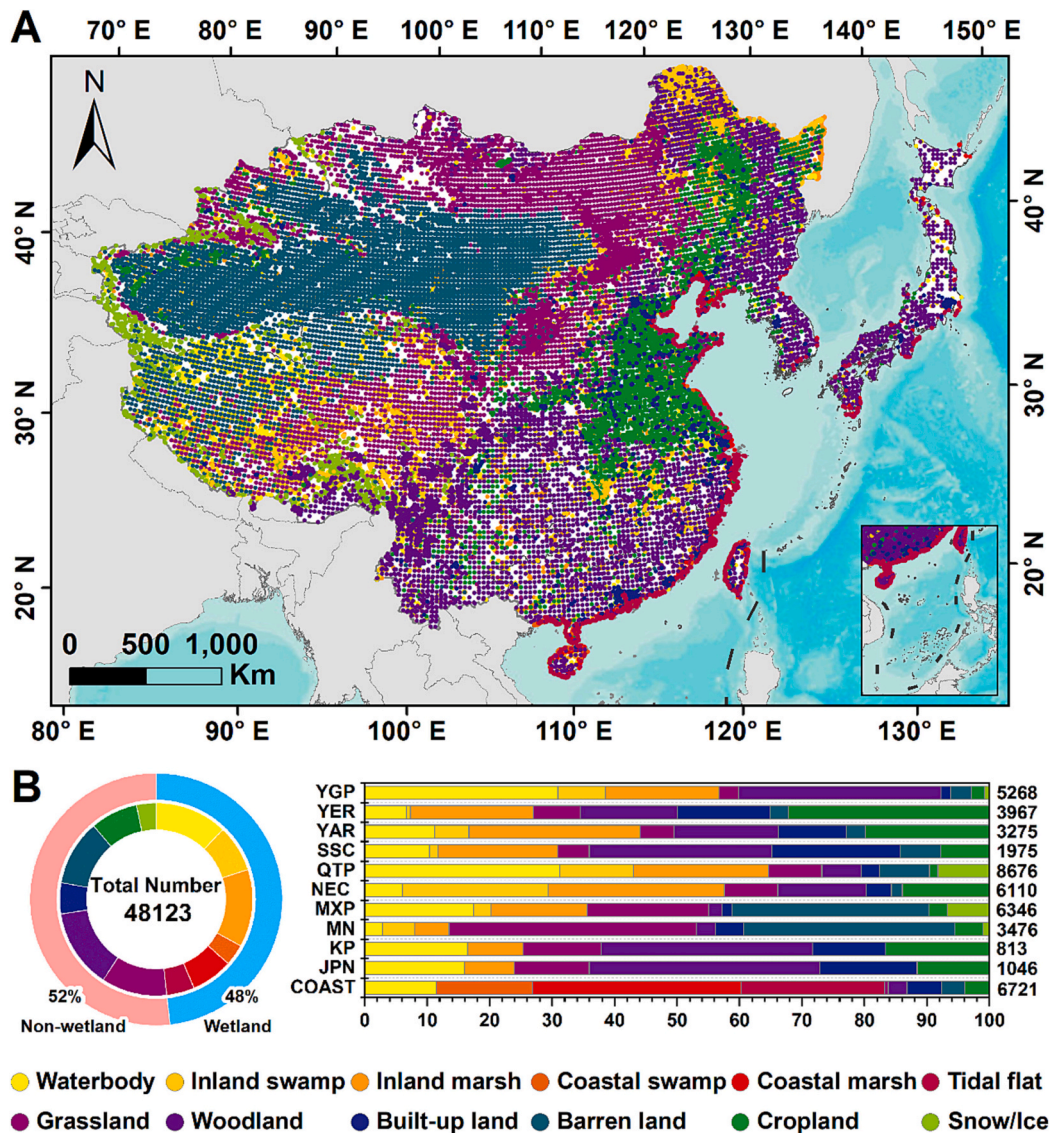


Fig. 7. Spatial distribution and number of training samples generated in this study, (A) presents the spatial distribution of training samples, and (B) shows the number of training samples for each ecoregion.

smaller SADs than other samples, which means more sample variability. This is mainly due to the spatial heterogeneity of vegetated wetlands, which can be addressed by regional strategy for large-scale wetland classification proposed in this study.

4.2. Classification accuracy of wetland categories

The assessment based on 41,742 validation samples showed that the generated 2021 wetland map of East Asia had an overall classification accuracy of 88.74% (Table 4), which is highly consistent with validation samples. The user's accuracy (UA) and producer's accuracy (PA) of every wetland category exceeded 78.46% and 80.09%, respectively. Lake category had the highest classification accuracy (UA: 91.85%, PA: 87.31%), followed by the river (UA: 91.17%, PA: 91.79%), and both inland marsh and coastal marsh had relatively lower accuracy with UA and PA <79% and 72%, respectively. The confusion matrix for each ecoregion showed that the overall accuracy (OA) of the wetland classification results was larger than 84% in each of the ecoregions. The MN had the highest accuracy (OA: 91.97%), followed by the MXP (OA: 91.22%), while the JPN (OA: 85.77%) and KP (OA: 84%) had slightly lower accuracies.

4.3. Area and distribution of wetlands in East Asia

Fig. 9 shows the up-to-date spatial pattern of wetlands in East Asia. Wetlands are widely distributed across East Asia with notable spatial heterogeneity, covering an estimated total area of 481,802.49 km², of which 68.26% were inland wetlands, followed by coastal wetlands (17.31%) and human-made wetlands (14.43%). Among the 12 sub-categories, inland marsh had the highest proportion (29.67%), followed by lake (20.98%), while coastal swamp had the lowest (0.07%). Among the inland wetland, inland marsh covered 142,932.35 km² (43.46%) with a concentration in NEC and QTP. Lakes and rivers accounted for 30.74% and 23.30% of the whole inland wetlands, widely observed throughout East Asia. In comparison, inland swamp comprised only 2.49%, predominantly in northern NEC. Among the coastal wetlands, the coastal waterbody has the largest area of 72,197.79 km² (86.55%). Tidal flats were widely distributed along the coast, accounting for 9.15% of the coastal wetlands, followed by coastal marsh being 3.93%. Coastal swamp comprised only 0.38%, primarily on China's southeastern coast. Approximately 80.87% of the total human-made wetlands in East Asia were reservoirs/ponds. Coastal aquaculture ponds with an area of 8676.67 km² were concentrated along China's

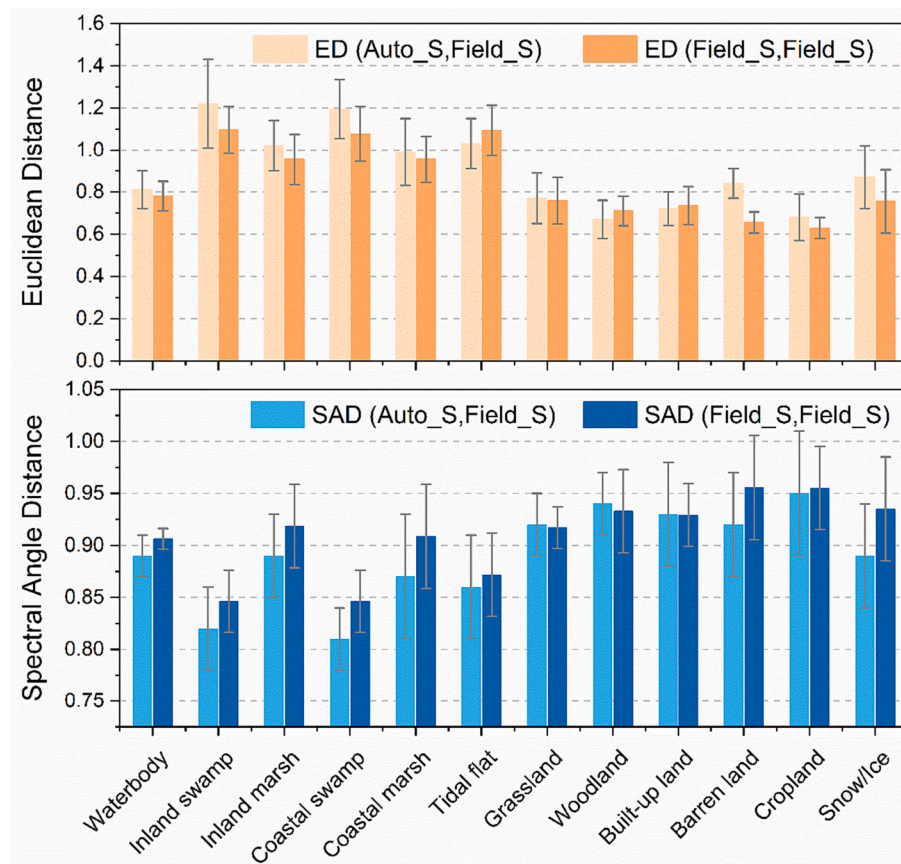


Fig. 8. Distance analysis between field samples (Field_S) and samples generated automatically in this study (Auto_S) for all spatiotemporal features. ED and SAD denote the Euclidean Distance and Spectral Angle Distance, respectively.

coast, occupying 12.48% of human-made wetlands. Canal/channel and salt pan distributed sparsely with an area proportion of only 5.03% and 1.62%.

Detailed measurements of wetlands for each country and ecoregion are presented in Fig. 9C-D and Table 5. China has 88.97% of the wetland resources in East Asia, and its wetland resources are composed of 70.78% inland wetlands, 14.93% human-made wetlands and 14.28% coastal wetlands. Among the seven ecoregions in China, the NEC has the largest wetland area (26.63%), containing 46.80% of China's inland marsh and over 84.28% of inland swamp. The QTP has widely distributed lakes (37.92%) and inland marshes (28.04%), comprising 19.48% of China's wetland area. The YAR has the highest proportion of reservoirs/ponds and tidal flats in China (27.63% and 38.96%), while the SSC has the most coastal swamps (75.57%), and the YER has the most coastal aquaculture ponds (40.55%) and salt pans (35.40%). Mongolia has 3.57% of East Asia's wetlands, of which 89.80% are inland wetlands consisting primarily of lakes (91.96%). Wetlands in Japan, South Korea, and North Korea are predominantly coastal wetlands, of which coastal waterbodies account for the largest proportion of 50.34%, 72.17%, and 55.62%, respectively. Note that the wetland results in the COAST were counted in the corresponding NEC, YER, YAR, SSC, KP, and JPN ecoregions, respectively.

5. Discussion

5.1. Two-stage classification for wetland mapping at continental scale

This research presents a novel two-stage classification for mapping wetlands at continental-scale. It is the first attempt on continental-scale wetland mapping at 10-m spatial resolution using the OBIA method. Using Sentinel-1/2 data and GEE platform, this novel two-stage

classification enabled the successful implementation of wetland mapping for five countries in East Asia. Specifically, the main improvements of this approach are as below.

First, we developed a novel method for automatically generating training samples to provide sufficient and reliable samples for continental-scale wetland mapping, significantly reducing the uncertainty of obtaining samples by visual interpretation in previous studies. Potential extents for sample generation were derived by combining multiple high-quality data, thereby significantly lowering the computational cost and inaccuracy of subsequent sample migration. In addition, by integrating the iForest with optimal spatiotemporal features, invalid samples that cannot be detected by visual interpretation or single features can be identified, ensuring the accuracy of sample migration. The iForest employed here has a lower time complexity and computational cost than distance-based and density-based outlier detection algorithms, making it more suitable for high-dimensional data (Liu et al., 2012), especially when combined with the Relief-F method in this study. As shown in Fig. 8, the developed method can automatically generate enough training samples that are highly consistent with field survey samples, as well as provide a feasible means of generating training samples for various large-scale classification studies.

Second, in addition to the commonly used features derived from a single image, we have incorporated many temporal features into the classification, which are essential for classifying wetlands as they highlight the dynamics of wetland and enhance their differences (Li et al., 2022a; Feng et al., 2022). Comparing inland marsh vs. grassland and inland swamp vs. woodland, for example, spatial features such as spectra, polarization, and texture are highly consistent (Fig. 4B), while there are apparent differences in temporal changes (Fig. 4C), which is the key to effectively distinguishing them. A >40% of selected optimal features for each ecoregion were temporal variables, as shown in

Table 4
Confusion matrix for accuracy assessment.

(a)				
Category I	Category II	Samples number	User's acc.	Producer's acc.
Inland wetland	River	1778	91.17 ± 1.31	91.79 ± 1.53
	Lake	1865	91.85 ± 1.24	87.31 ± 1.77
	Inland swamp	806	75.43 ± 2.97	69.97 ± 4.18
	Inland marsh	2051	78.94 ± 1.77	70.61 ± 5.24
Coastal wetland	Coastal swamp	908	79.19 ± 1.77	68.94 ± 3.13
	Coastal marsh	1599	76.17 ± 2.09	71.44 ± 4.24
	Tidal flat	501	80.44 ± 3.47	72.35 ± 3.73
	Coastal waterbody	103	93.20 ± 2.88	53.93 ± 5.88
Human-made wetland	Reservoir/pond	1258	87.92 ± 1.80	69.87 ± 1.72
	Canal/channel	196	77.04 ± 3.93	61.63 ± 5.27
	Salt pan	306	75.82 ± 3.81	66.10 ± 4.87
	Coastal aquaculture pond	707	80.76 ± 2.91	74.84 ± 3.71
Non-wetland		29,664	90.97 ± 0.33	90.97 ± 0.82
(b)				
Region	Wetland samples number		User's acc.	Producer's acc.
YGP	1239	71.78 ± 1.80	83.28 ± 2.11	88.93 ± 0.12
YER	1283	86.36 ± 1.95	80.44 ± 1.82	91.62 ± 0.02
YAR	1360	81.07 ± 1.71	78.75 ± 1.25	88.51 ± 0.02
SSC	1211	81.16 ± 1.73	81.09 ± 1.82	89.75 ± 0.02
QTP	1566	67.99 ± 1.63	81.41 ± 1.58	86.58 ± 0.02
NEC	1366	71.35 ± 1.89	81.74 ± 1.18	86.93 ± 0.03
MXP	1209	88.86 ± 1.88	79.16 ± 2.03	90.22 ± 0.02
MN	1005	83.35 ± 2.39	77.71 ± 1.85	89.97 ± 0.02
KP	917	78.93 ± 1.34	76.17 ± 1.57	84.00 ± 0.03
JPN	922	78.46 ± 2.37	80.38 ± 1.09	85.77 ± 0.03
Summary	12,078	78.46 ± 1.28	80.08 ± 0.57	88.74 ± 0.03

Fig. 10A, indicating that they were crucial for wetland classification. In addition, it can be seen that among the selected optimal features in each ecoregion, the temporal features generally had higher weights than other common features, meaning that they were more important for accurate classification, especially in the KP, MXP, and QTP. Our results show that adding various temporal features can enhance the overall classification accuracy by 1% to 5% (average 2.35%) (Fig. 10B).

Third, a two-stage classification developed in this study ensured the accuracy of wetland mapping in East Asia. It is challenging to accurately classify all categories of wetlands at once using sample-based machine learning methods, as many wetlands have similar spectral, textural, and temporal features, such as the lake, ponds/reservoirs, and coastal aquaculture ponds in this study. The two-stage classification effectively resolves this issue. Based on the initial classification results generated by the object-based RF algorithm, a hierarchical decision tree based on multi-features (e.g., shape, texture, topography, and temporal variation) is constructed for the secondary classification, achieving fine wetland classification. Additionally, this study applied a novel sub-regional strategy to divide the study area into various ecoregions and then train the classification models independently. This strategy could significantly minimize the computational memory required for model training, facilitate the implementation of large-scale wetland mapping using the two-stage classification, and greatly reduce misclassification

between similar landscapes.

The accuracies of wetland mapping in this study were inevitably affected by some factors. First, some ecoregions suffer from uneven sample size, which might lead to abnormal classification. To prevent this issues during the classification process, we can only rely on manual sample size adjustment to maintain sample balance. While automatically generating a sufficient number of training samples, it is necessary to design strategies for maintaining the evenly of samples' quantity and distribution (Gong et al., 2019; Huang et al., 2020). Second, given the strong spatial heterogeneity and spatio-temporal dynamics of wetland landscapes, the regional strategy and optimal segmentation threshold adopted in this study may still introduce uncertainties in the wetland delineation result, especially in the adjacent areas between task grids. More advanced image segmentation algorithms and automated methods to determine the optimal segmentation threshold should be explored in future studies to reduce the potential discrepancies in the resulting wetland maps across different regions. In addition, numerous studies have revealed that multi-year, continuous monitoring of the spatio-temporal dynamics of wetlands have greater practical value for the protection and wise use of wetlands (Gong et al., 2010; Mao et al., 2022). Thus, studies for interannual dynamics of wetlands over a large-scale remain need to further explore in future studies.

5.2. High resolution wetlands map of East Asia

Fig. 11 compares the resulting wetland map in this study with other wetland datasets (Table 1), including the 30-m national wetland map of China in 2015 (CAS_Wetlands), 10-m products of global land cover in 2021 (ESA_WorldCover), and three national maps of tidal flats, mangroves, and coastal aquaculture ponds of China (e.g., 10-m China_Tidal Flat map in 2019, 30-m CAS_Mangroves map in 2015, and 10-m China_CAP map in 2021). To minimize the negative impact of different generated years on comparisons between datasets, we identified regions with low inter-annual dynamic variation for the final contrast. Compared to the CAS_Wetlands, this study provides the up-to-date wetland map of 2021 with a finer spatial resolution of 10-m. In addition, this study provides a more consistent extent of wetlands compared to ESA_WorldCover, which can be primarily related to their distinct classification methods. ESA_WorldCover was generated using pixel-based classification approach, which was influenced by the "salt and pepper" effect, especially for inland and coastal marshes. In contrast, this study uses an object-based classification method that combines super-pixel segmentation and RF classification to reduce such noise and provide more accurate mapping. We also compared the area of three coastal wetland categories (tidal flat, coastal swamp, and coastal aquaculture pond) with those from three existing datasets (China_Tidal Flat, CAS_Mangroves, and China_CAP) for each coastal province of China, respectively (Fig. 9B). Our results were highly consistent ($p < 0.001$) with all these existing datasets. The differences in area may stem from the different methods of data generation. The coastal swamp area estimated in this study was significantly larger than that of CAS_Mangroves for all provinces (Zhejiang, Fujian, Guangdong, Guangxi, Hainan and Taiwan). This discrepancy can be attributed to two main factors: firstly, CAS_Mangroves only covers the single type of coastal swamp, namely mangroves, while this study also includes other categories. Secondly, the difference in resolution also affects the area estimate, and the finer resolution of this study allows for more detailed information capture.

5.3. Implication of continental-scale wetland map with finer spatial resolution

At a 10-m spatial resolution, this study generates the first wetland map for East Asia (EA_Wetlands). Such continental-scale wetland distribution product with fine spatial resolution and multiple categories will be of great potential applications in scientific research and

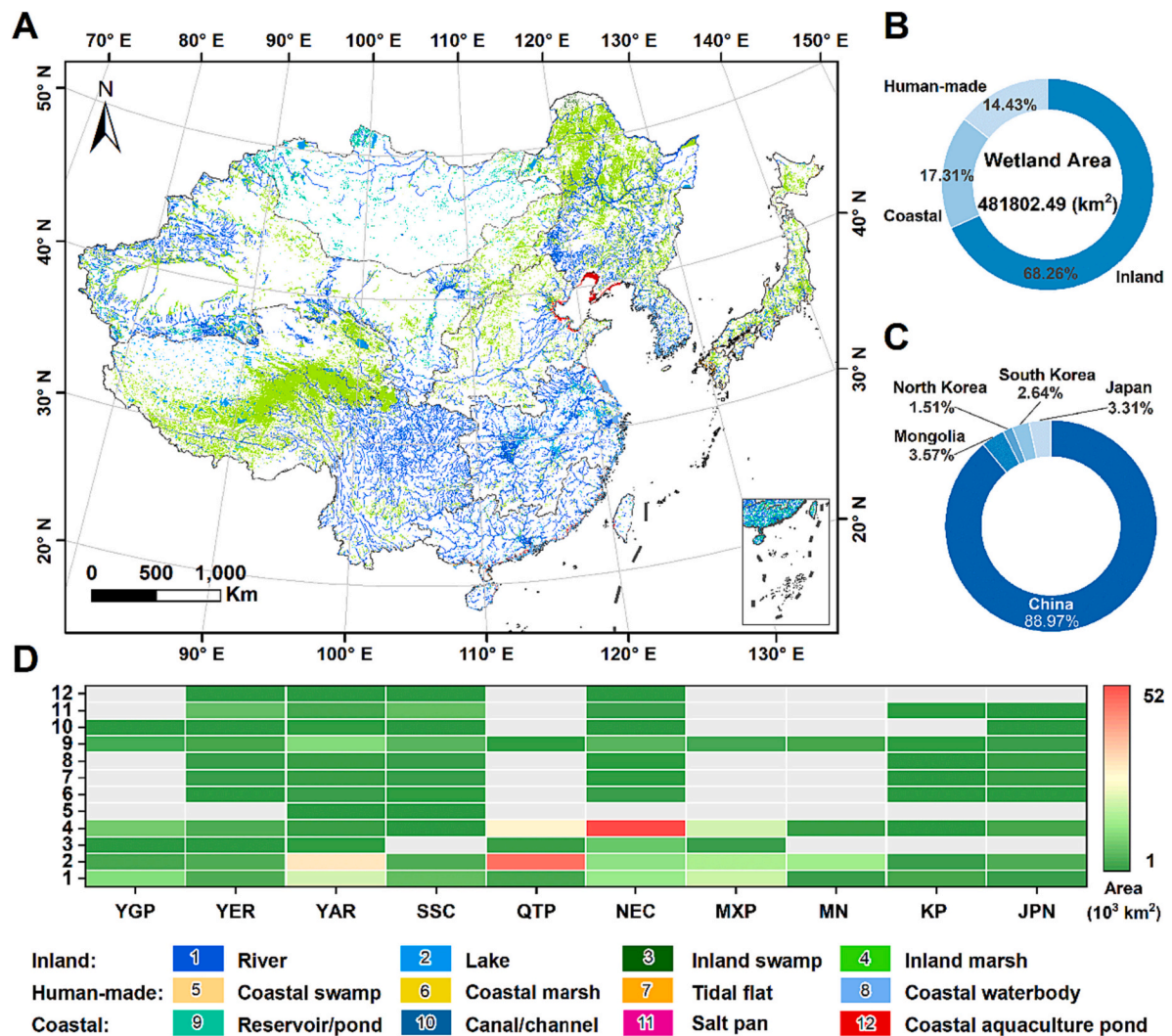


Fig. 9. Distribution and areal statistics of wetlands for EA in 2021, (A) presents the spatial distribution and area in latitude of wetlands, (B), (C), and (D) show wetland area statistics for different categories, countries, and ecoregions.

Table 5

Area of various wetland categories in five East Asian countries.

Category I	Category II	China	Mongolia	North Korea	South Korea	Japan	Summary
Inland wetland	Lake	73,203.16	777.65	735.78	716.74	1210.80	76,644.13
	River	83,091.61	14,217.80	477.70	376.98	2914.84	101,078.93
	Inland swamp	7965.08	132.59	10.26	21.16	75.39	8204.48
	Inland marsh	139,167.10	332.73	897.21	1104.26	1431.04	142,932.35
	Total	303,426.95	15,460.77	2120.95	2219.14	5632.06	328,859.88
Coastal wetland	Coastal swamp	302.00	0.00	8.57	1.45	3.57	315.59
	Coastal marsh	3096.35	0.00	38.17	50.24	91.79	3276.55
	Tidal flat	6894.29	0.00	59.55	189.65	486.44	7629.94
	Coastal waterbody	50,963.25	0.00	4038.33	9175.34	8020.86	72,197.79
	Total	61,255.89	0.00	4144.62	9416.69	8602.67	83,419.87
Human-made wetland	Reservoir/pond	50,792.60	1750.59	959.66	1049.07	1670.55	56,222.47
	Canal/channel	3453.85	5.29	2.61	13.31	21.52	3496.59
	Coastal aquaculture pond	8628.80	0.00	31.87	13.82	2.17	8676.67
	Salt pan	1122.52	0.00	1.02	1.19	2.27	1127.01
	Total	50,792.60	1750.59	959.66	1049.07	1670.55	69,522.74
Summary		428,680.62	17,216.65	7260.74	12,713.23	15,931.25	481,802.49

sustainable management including biodiversity conservation, migratory bird habitat assessment, and carbon storage or sink estimation. In addition to accurately estimating the total wetland area in East Asia, the EA Wetlands also provides the precise extent of 3 broad categories and 12 sub-categories of wetlands. Biodiversity conservation and sustainable

ecosystem management in East Asia will benefit significantly from such detailed wetland classification. For example, fine spatial distribution information of swamp and marsh in coastal and inland areas is helpful for better understanding their ecological functions and services, and is of great importance for carbon sink studies in terrestrial ecosystems. The

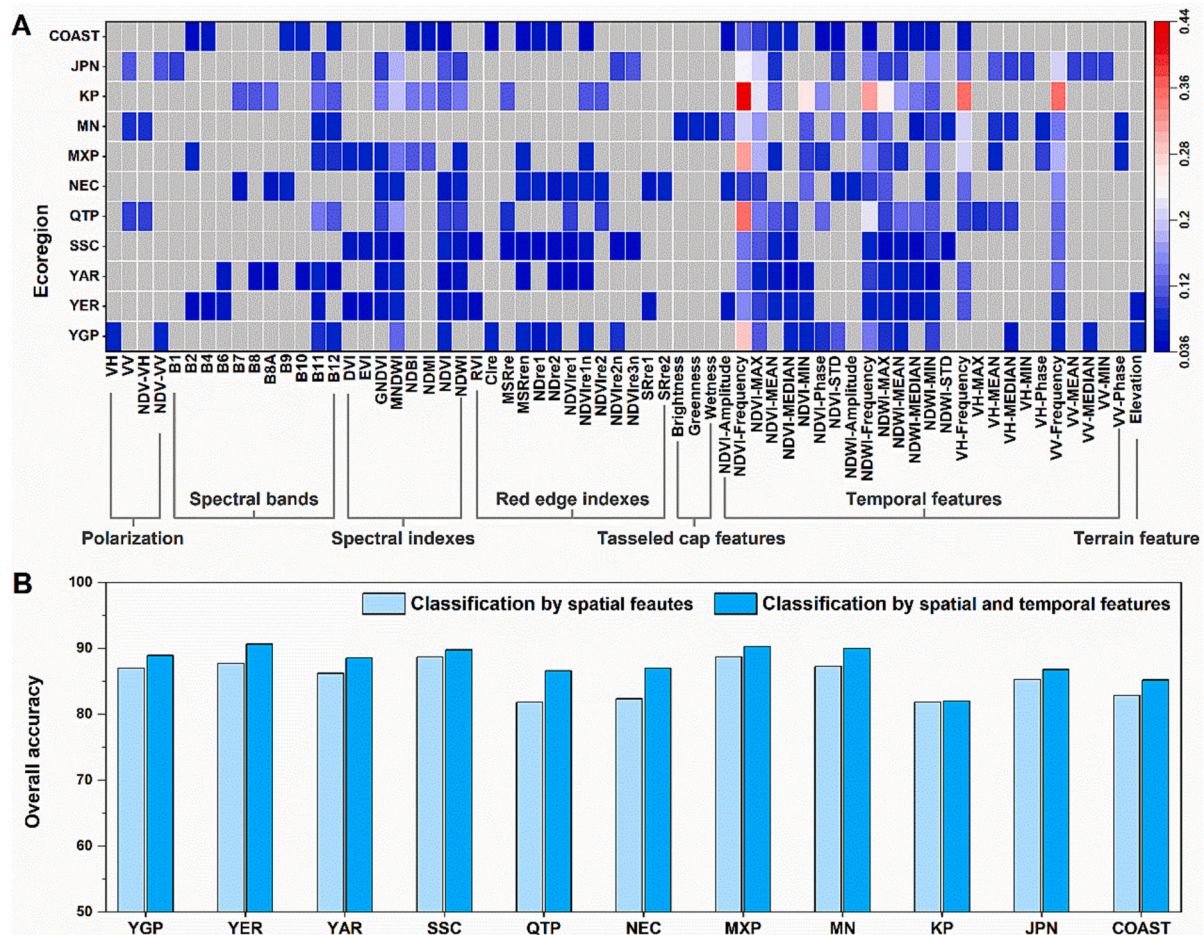


Fig. 10. Optimal features selection result and the overall accuracy change caused by temporal features. (A) shows the optimal feature selection result for each ecoregion, where X-axis represents the selected optimal features and the Y-axis represents the ecoregions. The colored squares indicate the weights of the selected features, and the gray squares indicate that the feature is not selected. (B) presents the accuracy change caused by the adding of various temporal features.

various natural and human-made wetlands in urban areas can be used for evaluating the conservation and utilization status of urban wetlands, providing invaluable information for sustainable urban planning and management (Wang et al., 2022). In the coastal zone, the accurate delimitation of tidal flats, which providing dominant foraging habitats for migratory birds, could provide data support for conservation of migratory water birds on the East Asia-Australia Flyway (EAAF) (Jia et al., 2021; Li et al., 2022b; Qiu et al., 2022). And the latest extent of aquaculture ponds and salt pans can be used for monitoring the development intensity of coastal zones and supporting coastal wetland protection and restoration decisions (Ren et al., 2019; Wang et al., 2023). Additionally, EA Wetlands also provides a critical reference for evaluating the implementation of the Ramsar Convention and SDGs in China and other East Asia parties (Mao et al., 2021). According to the Ramsar Convention, 154 wetland sites in East Asia have been included in the list of wetlands with international importance to date, and China has the most wetland cities in the world. EA Wetlands can provide the latest data support on the status of wetlands in these important wetland sites and wetland cities. Among various wetland-relevant indicators of SDGs, SDG 6.6.1 focuses on tracking changes over time in water-related ecosystems, and the method developed for continental-scale wetland mapping in this study can directly contribute to it.

6. Conclusions

Using the Sentinel-1/2 time series imagery and the GEE platform, we developed a novel two-stage wetland mapping framework that

integrates object-based RF and hierarchical decision tree classification, and firstly generated the up-to-date 10-m resolution wetland map of East Asia with 3 broad categories and 12 sub-categories. Various spatio-temporal features and an effective method for automatically generating samples were incorporated into the fine classification of wetlands, further ensuring the classification accuracy. The resulting wetlands map of East Asia has an overall classification accuracy of 88.74%, revealing an estimated area being 481,802.49 km² for this continent, and a primary distribution in China's NEC and QTP. Among all wetlands, 68.26% are inland wetlands, 17.31% are coastal wetland, and 14.43% are human-made wetland, whilst inland marsh had the highest proportion (29.67%). China has the largest wetland resources (88.97%) and North Korea has the smallest (1.51%) among five East Asian countries. The novel method and resulting wetland product could contribute directly to evaluating targets of SDGs and provide a critical reference for achieving the fine global wetland map.

CRedit authorship contribution statement

Ming Wang: Methodology, Software, Writing – original draft. **Dehua Mao:** Conceptualization, Validation, Funding acquisition, Writing – review & editing. **Yeqiao Wang:** Writing – review & editing, Validation. **Xiangming Xiao:** Writing – review & editing, Validation. **Hengxing Xiang:** Data curation, Validation. **Kaidong Feng:** Data curation, Validation. **Ling Luo:** Writing – review & editing. **Mingming Jia:** Writing – review & editing. **Kaishan Song:** Writing – review & editing. **Zongming Wang:** Conceptualization, Writing – review &

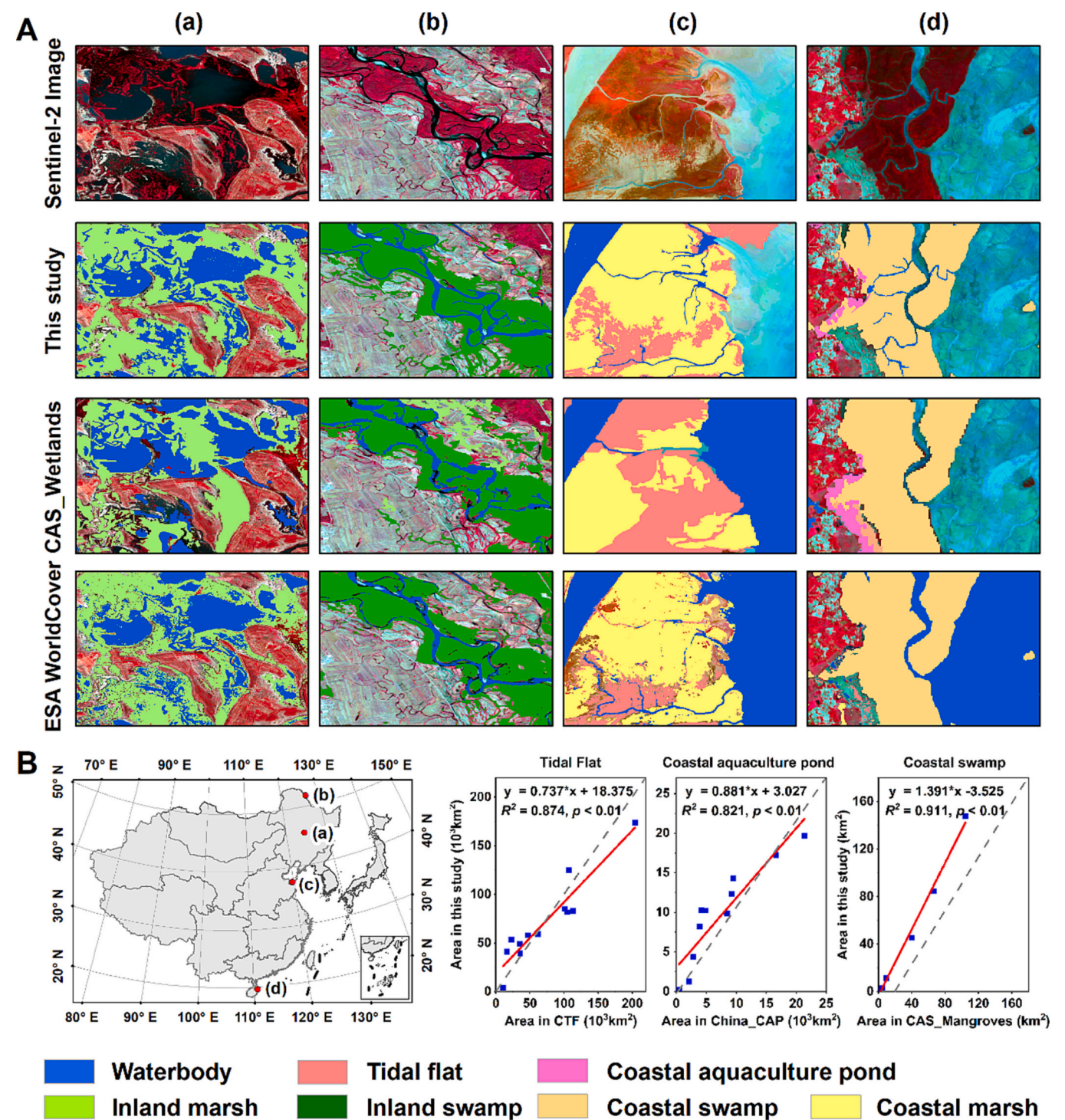


Fig. 11. Comparison with other wetland maps. A presents the comparison between our result and two wetland datasets (CAS_Wetlands and ESA_WorldCover), B shows the correlation between the estimated areas of our result and various coastal wetlands, including China_Tidal Flat, CAS_Mangroves, and China CAP.

editing, Validation.

Declaration of Competing Interest

The authors declare that they have no known competing financial interests or personal relationships that could have appeared to influence the work reported in this paper.

Data availability

Data will be made available on request.

Acknowledgments

This research was jointly funded by the National Natural Science Foundation of China (42171379, 42222103, and 42101379), the Science and Technology Development Program of Jilin Province, China (20210101396JC), the Youth Innovation Promotion Association of

Chinese Academy of Sciences (2017277, 2021227), and the Young Scientist Group Project of Northeast Institute of Geography and Agroecology, Chinese Academy of Sciences (2022QNXX03). Xiangming Xiao was supported by the U.S. National Science Foundation (1911955).

References

- Achanta, R., Süsstrunk, S., 2017. Superpixels and polygons using simple non-iterative clustering. *IEEE Conference on Computer Vision and Pattern Recognition (CVPR)* 2017, 4895–4904. <https://doi.org/10.1109/CVPR.2017.520>.
- Amante, C., Eakins, B., 2009. ETOPO1 1 Arc-Minute Global Relief Model: Procedures, data sources and analysis. <https://doi.org/10.7289/V5C8276M>.
- Ashourloo, D., Nematollahi, H., Huete, A., Aghighi, H., Azadbakht, M., Shahrabi, H.S., Goodarzdahshi, S., 2022. A new phenology-based method for mapping wheat and barley using time-series of Sentinel-2 images. *Remote Sens. Environ.* 280, 113206 <https://doi.org/10.1016/j.rse.2022.113206>.
- Baghdadi, N., Bernier, M., Gauthier, R., Neeson, I., 2001. Evaluation of C-band SAR data for wetlands mapping. *Int. J. Remote Sens.* 22 (1), 71–88. <https://doi.org/10.1080/014311601750038857>.
- Betheder, J., Gond, V., Frappart, F., Baghdadi, N.N., Briant, G., Bartholomé, E., 2014. Mapping of Central Africa forested wetlands using remote sensing. *IEEE J. Select. Top. Appl. Earth Observ. Remote Sens.* 7 (2), 531–542. <https://doi.org/10.1109/JSTARS.2013.2269733>.
- Blaschke, T., 2010. Object based image analysis for remote sensing. *ISPRS J. Photogramm. Remote Sens.* 65 (1), 2–16. <https://doi.org/10.1016/j.isprsjprs.2009.06.004>.
- Brown, C.F., Brumby, S.P., Guzder-Williams, B., Birch, T., Hyde, S.B., Mazzariello, J., Czerwinski, W., Pasquarella, V.J., Haertel, R., Ilyushchenko, S., Schwehr, K., Weisse, M., Stolle, F., Hanson, C., Guinan, O., Moore, R., Tait, A.M., 2022. Dynamic world, near real-time global 10 m land use land cover mapping. *Scientific Data* 9 (1). <https://doi.org/10.1038/s41597-022-01307-4>. Article 1.
- Bunting, P., Rosenqvist, A., Lucas, R.M., Rebelo, L.-M., Hilarides, L., Thomas, N., Hardy, A., Itoh, T., Shimada, M., Finlayson, C.M., 2018. The global mangrove Watch—anew 2010 global baseline of mangrove extent. *Remote Sens.* 10 (10) <https://doi.org/10.3390/rs10101669>. Article 10.
- Davidson, N.C., Davidson, N.C., 2014. How much wetland has the world lost? Long-term and recent trends in global wetland area. *Mar. Freshw. Res.* 65 (10), 934–941. <https://doi.org/10.1071/MF14173>.
- Feng, K., Mao, D., Qiu, Z., Zhao, Y., Wang, Z., 2022. Can time-series sentinel images be used to properly identify wetland plant communities? *GIScience Remote Sens.* 59 (1), 2202–2216. <https://doi.org/10.1080/15481603.2022.2156064>.
- Gong, P., Li, X., Wang, J., Bai, Y., Chen, B., Hu, T., Liu, X., Xu, B., Yang, J., Zhang, W., Zhou, Y., 2020. Annual maps of global artificial impervious area (GAIA) between 1985 and 2018. *Remote Sens. Environ.* 236, 111510 <https://doi.org/10.1016/j.rse.2019.111510>.
- Gong, P., Liu, H., Zhang, M., Li, C., Wang, J., Huang, H., Clinton, N., Ji, L., Li, W., Bai, Y., Chen, B., Xu, B., Zhu, Z., Yuan, C., Ping Suen, H., Guo, J., Xu, N., Li, W., Zhao, Y., Song, L., 2019. Stable classification with limited sample: transferring a 30-m resolution sample set collected in 2015 to mapping 10-m resolution global land cover in 2017. *Sci. Bull.* 64 (6), 370–373. <https://doi.org/10.1016/j.scib.2019.03.002>.
- Gong, P., Niu, Z., Cheng, X., Zhao, K., Zhou, D., Guo, J., Liang, L., Wang, X., Li, D., Huang, H., Wang, Y., Wang, K., Li, W., Wang, X., Ying, Q., Yang, Z., Ye, Y., Li, Z., Zhuang, D., Yan, J., 2010. China's wetland change (1990–2000) determined by remote sensing. *Sci. China Earth Sci.* 53 (7), 1036–1042. <https://doi.org/10.1007/s11430-010-4002-3>.
- Hosseini, B., Mahdianpari, M., Brisco, B., Mohammadimanesh, F., Salehi, B., 2022. WetNet: a spatial-temporal ensemble deep learning model for wetland classification using Sentinel-1 and Sentinel-2. *IEEE Trans. Geosci. Remote Sens.* 60, 1–14. <https://doi.org/10.1109/TGRS.2021.3113856>.
- Huang, H., Wang, J., Liu, C., Liang, L., Li, C., Gong, P., 2020. The migration of training samples towards dynamic global land cover mapping. *ISPRS J. Photogramm. Remote Sens.* 161, 27–36. <https://doi.org/10.1016/j.isprsjprs.2020.01.010>.
- Jakubauskas, M.E., Legates, D.R., Kastens, J.H., 2002. Crop identification using harmonic analysis of time-series AVHRR NDVI data. *Comput. Electron. Agric.* 37 (1), 127–139. [https://doi.org/10.1016/S0168-1699\(02\)00116-3](https://doi.org/10.1016/S0168-1699(02)00116-3).
- Jia, M., Wang, Z., Mao, D., Ren, C., Wang, C., Wang, Y., 2021. Rapid, robust, and automated mapping of tidal flats in China using time series Sentinel-2 images and Google Earth Engine. *Remote Sens. Environ.* 255, 112285 <https://doi.org/10.1016/j.rse.2021.112285>.
- Jia, M., Wang, Z., Zhang, Y., Mao, D., Wang, C., 2018. Monitoring loss and recovery of mangrove forests during 42 years: the achievements of mangrove conservation in China. *Int. J. Appl. Earth Obs. Geoinf.* 73, 535–545. <https://doi.org/10.1016/j.jag.2018.07.025>.
- Jin, H., Huang, C., Lang, M.W., Yeo, I.-Y., Stehman, S.V., 2017. Monitoring of wetland inundation dynamics in the Delmarva Peninsula using landsat time-series imagery from 1985 to 2011. *Remote Sens. Environ.* 190, 26–41. <https://doi.org/10.1016/j.rse.2016.12.001>.
- Kaplan, G., Avdan, U., 2018. Sentinel-1 and Sentinel-2 data fusion for wetlands mapping: Balıkdami, Turkey. <https://doi.org/10.5194/isprs-archives-XLII-3-729-2018>.
- Kononenko, I., 1994. Estimating attributes: Analysis and extensions of RELIEF. In: Bergadano, L. De Raedt (Ed.), *Machine Learning: ECML-94*. Springer, pp. 171–182. https://doi.org/10.1007/3-540-57868-4_57.
- Kotsiantis, S.B., 2013. Decision trees: a recent overview. *Artif. Intell. Rev.* 39 (4), 261–283. <https://doi.org/10.1007/s10462-011-9272-4>.
- Lehner, B., Döll, P., 2004. Development and validation of a global database of lakes, reservoirs and wetlands. *J. Hydrol.* 296 (1), 1–22. <https://doi.org/10.1016/j.jhydrol.2004.03.028>.
- Li, A., Song, K., Chen, S., Mu, Y., Xu, Z., Zeng, Q., 2022. Mapping african wetlands for 2020 using multiple spectral, geo-ecological features and Google Earth Engine. *ISPRS J. Photogramm. Remote Sens.* 193, 252–268. <https://doi.org/10.1016/j.isprsjprs.2022.09.009>.
- Li, H., Mao, D., Wang, Z., Huang, X., Li, L., Jia, M., 2022. Invasion of *Spartina alterniflora* in the coastal zone of mainland China: control achievements from 2015 to 2020 towards the sustainable development goals. *J. Environ. Manag.* <https://doi.org/10.1016/j.jenvman.2022.116242>.
- Liu, F.T., Ting, K.M., Zhou, Z.-H., 2012. Isolation-based anomaly detection. *ACM Trans. Knowl. Discov. Data* 6(1), 3: 1–39. <https://doi.org/10.1145/2133360.2133363>.
- Liu, Y., Zhang, H., Zhang, M., Cui, Z., Lei, K., Zhang, J., Yang, T., Ji, P., 2022. Vietnam wetland cover map: using hydro-periods Sentinel-2 images and Google Earth Engine to explore the mapping method of tropical wetland. *Int. J. Appl. Earth Obs. Geoinf.* 115, 103122 <https://doi.org/10.1016/j.jag.2022.103122>.
- Mahdianpari, M., Salehi, B., Mohammadimanesh, F., Brisco, B., Homayouni, S., Gill, E., Delancey, E.R., Bourgeau-Chavez, L., 2020. Big data for a big country: the first generation of Canadian wetland inventory map at a spatial resolution of 10-m using Sentinel-1 and Sentinel-2 data on the Google Earth Engine cloud computing platform. *Can. J. Remote. Sens.* 46 (1), 15–33. <https://doi.org/10.1080/07038992.2019.1711366>.
- Mao, D., Wang, Z., Du, B., Li, L., Tian, Y., Jia, M., Zeng, Y., Song, K., Jiang, M., Wang, Y., 2020. National wetland mapping in China: a new product resulting from object-based and hierarchical classification of landsat 8 OLI images. *ISPRS J. Photogramm. Remote Sens.* 164, 11–25. <https://doi.org/10.1016/j.isprsjprs.2020.03.020>.
- Mao, D., Wang, Z., Wang, Y., Choi, C.-Y., Jia, M., Jackson, M.V., Fuller, R.A., 2021. Remote observations in China's Ramsar sites: wetland dynamics, anthropogenic threats, and implications for sustainable development goals. *J. Remote Sens.* 2021, 9849343. <https://doi.org/10.34133/2021/9849343>.
- Mao, D., Wang, Z., Wu, J., Wu, B., Zeng, Y., Song, K., Yi, K., Luo, L., 2018. China's wetlands loss to urban expansion. *Land Degrad. Dev.* 29 (8), 2644–2657. <https://doi.org/10.1002/ldr.2939>.
- Mao, D., Yang, H., Wang, Z., Song, K., Thompson, J.R., Flower, R.J., 2022. Reverse the hidden loss of China's wetlands. *Science* 376 (6597), 1061. <https://doi.org/10.1126/science.adc8833>.
- Matsushita, B., Fukushima, T., 2009. Methods for retrieving hydrologically significant surface parameters from remote sensing: a review for applications to East Asia region. *Hydrol. Process.* 23 (4), 524–533. <https://doi.org/10.1002/hyp.7182>.
- Mulligan, M., van Soesbergen, Saenz, L., 2020. GOODD, a global dataset of more than 38,000 georeferenced dams. *Scientific Data*. <http://www.nature.com/scientificdata>.
- Murray, N.J., Phinn, S.R., DeWitt, M., Ferrari, R., Johnston, R., Lyons, M.B., Clinton, N., Thau, D., Fuller, R.A., 2019. The global distribution and trajectory of tidal flats. *Nature* 565 (7738). <https://doi.org/10.1038/s41586-018-0805-8>. Article 7738.
- Olofsson, P., Foody, G.M., Herold, M., Stehman, S.V., Woodcock, C.E., Wulder, M.A., 2014. Good practices for estimating area and assessing accuracy of land change. *Remote Sens. Environ.* 148, 42–57. <https://doi.org/10.1016/j.rse.2014.02.015>.
- Otsu, N., 1979. A threshold selection method from gray-level histograms. *IEEE Trans. Syst. Man Cybernet.* 9 (1), 62–66. <https://doi.org/10.1109/TSMC.1979.4310076>.
- Pekel, J.-F., Cottam, A., Gorelick, N., Belward, A.S., 2016. High-resolution mapping of global surface water and its long-term changes. *Nature* 540 (7633). <https://doi.org/10.1038/nature20584>. Article 7633.
- Peng, K., Jiang, W., Hou, P., Wu, Z., Ling, Z., Wang, X., Niu, Z., Mao, D., 2023. Continental-scale wetland mapping: a novel algorithm for detailed wetland types classification based on time series Sentinel-1/2 images. *Ecol. Indic.* 148, 110113 <https://doi.org/10.1016/j.ecolind.2023.110113>.
- Qiu, Z., Mao, D., Feng, K., Wang, M., Xiang, H., Wang, Z., 2022. High-resolution mapping changes in the invasion of *spartina alterniflora* in the Yellow River Delta. *IEEE J. Select. Top. Appl. Earth Observ. Remote Sens.* 15, 6445–6455. <https://doi.org/10.1109/JSTARS.2022.3193293>.
- Ren, C., Wang, Z., Zhang, Y., Zhang, B., Chen, L., Xi, Y., Xiao, X., Doughty, R.B., Liu, M., Jia, M., Mao, D., Song, K., 2019. Rapid expansion of coastal aquaculture ponds in China from Landsat observations during 1984–2016. *Int. J. Appl. Earth Obs. Geoinf.* 82, 101902 <https://doi.org/10.1016/j.jag.2019.101902>.
- Tana, G., Letu, H., Cheng, Z., Tateishi, R., 2013. Wetlands mapping in North America by decision rule classification using MODIS and ancillary data. *IEEE J. Select. Top. Appl. Earth Observ. Remote Sens.* 6 (6), 2391–2401. <https://doi.org/10.1109/JSTARS.2013.2249499>.
- Tassi, A., Vizzari, M., 2020. Object-oriented LULC classification in Google earth engine combining SNIC, GLCM, and machine learning algorithms. *Remote Sens.* 12 (22) <https://doi.org/10.3390/rs12223776>. Article 22.
- Thenkabail, P.S., Knox, J.W., Ozdogan, M., Gumma, M.K., Congalton, R.G., Wu, Z.T., Milesi, C., Finkral, A., Marshall, M., Mariotto, I., SongCai, Y., Giri, C., Nagler, P., 2012. Assessing future risks to agricultural productivity, water resources and food security: how can remote sensing help? *PE&RS, Photogramm. Eng. Remote Sens.* 78 (8), 773–782.
- Wang, M., Mao, D., Wang, Y., Song, K., Yan, H., Jia, M., Wang, Z., 2022. Annual wetland mapping in Metropolis by temporal sample migration and random Forest classification with time series Landsat data and Google earth engine. *Remote Sens.* 14(13), Article 13 <https://doi.org/10.3390/rs14133191>.
- Wang, M., Mao, D., Xiao, X., Song, K., Jia, M., Ren, C., Wang, Z., 2023. Interannual changes of coastal aquaculture ponds in China at 10-m spatial resolution during

- 2016–2021. *Remote Sens. Environ.* 284, 113347 <https://doi.org/10.1016/j.rse.2022.113347>.
- Wang, X., Xiao, X., Zou, Z., Hou, L., Qin, Y., Dong, J., Doughty, R.B., Chen, B., Zhang, X., Chen, Y., Ma, J., Zhao, B., Li, B., 2020. Mapping coastal wetlands of China using time series Landsat images in 2018 and Google earth engine. *ISPRS J. Photogramm. Remote Sens.* 163, 312–326. <https://doi.org/10.1016/j.isprsjprs.2020.03.014>.
- Wang, Y., Makedon, F., 2004. In: Application of Relief-F feature filtering algorithm to selecting informative genes for cancer classification using microarray data. *Proceedings. 2004 IEEE Computational Systems Bioinformatics Conference, 2004. CSB 2004*, pp. 497–498. <https://doi.org/10.1109/CSB.2004.1332474>.
- Wang, Z., Wu, J., Madden, M., Mao, D., 2012. China's wetlands: conservation plans and policy impacts. *Ambio* 41 (7), 782–786. <https://doi.org/10.1007/s13280-012-0280-7>.
- Wu, B., 2014. Land cover changes of China from 2000 to 2010. *Quat Sci* 34, 723–731.
- Yommy, A.S., Liu, R., Shuang, Wu, 2015. In: SAR Image Despeckling Using Refined Lee Filter. 2015 7th International Conference on Intelligent Human-Machine Systems and Cybernetics, 2, pp. 260–265. <https://doi.org/10.1109/IHMSC.2015.236>.
- Zanaga, D., Van De Kerchove, R., Daems, D., De Keersmaecker, W., Brockmann, C., Kirches, G., Wevers, J., Cartus, O., Santoro, M., Fritz, S., Lesiv, M., Herold, M., Tsendbazar, N.-E., Xu, P., Ramoino, F., Arino, O., 2022. ESA WorldCover 10 m 2021 v200 [Data set]. Zenodo. <https://doi.org/10.5281/zenodo.7254221>.
- Zedler, J.B., Kercher, S., 2005. WETLAND RESOURCES: status, trends, ecosystem services, and restorability. *Annu. Rev. Environ. Resour.* 30 (1), 39–74. <https://doi.org/10.1146/annurev.energy.30.050504.144248>.
- Zhang, Z., Xu, N., Li, Y., Li, Y., 2022. Sub-continental-scale mapping of tidal wetland composition for East Asia: a novel algorithm integrating satellite tide-level and phenological features. *Remote Sens. Environ.* 269, 112799 <https://doi.org/10.1016/j.rse.2021.112799>.
- Zhao, C., Qin, C.-Z., Wang, Z., Mao, D., Wang, Y., Jia, M., 2022. Decision surface optimization in mapping exotic mangrove species (*Sonneratia apetala*) across latitudinal coastal areas of China. *ISPRS J. Photogramm. Remote Sens.* 193, 269–283. <https://doi.org/10.1016/j.isprsjprs.2022.09.011>.
- Zhou, J., Jia, L., Menenti, M., 2015. Reconstruction of global MODIS NDVI time series: performance of harmonic ANalysis of time series (HANTS). *Remote Sens. Environ.* 163, 217–228. <https://doi.org/10.1016/j.rse.2015.03.018>.
- Zou, Q., Ni, L., Zhang, T., Wang, Q., 2015. Deep learning based feature selection for remote sensing scene classification. *IEEE Geosci. Remote Sens. Lett.* 12 (11), 2321–2325. <https://doi.org/10.1109/LGRS.2015.2475299>.